[3] Fermilab E791 Collaboration, "Search for the pentaquark via the $P^0_{\bar{c}s} \rightarrow \phi\pi p$ decay"; to be published in Phys. Rev. Lett. (1998).

[20] S. MayTal Beck *et al.*, Proc. of the 8th Meeting, Div. of Particles and Fields of the Am. Phys. Soc., S. Seidel *ed.*, World Scientific (1994), p. 1177.

[21] D. Ashery, Hyperfine Interactions **103** 253 (1996).

[22] Particle Data Group, Phys. Rev. **D54** (1996).

[23] J.C. Anjos *et al.*, 1988, E791: Continued study of Heavy Flavors at TPL, A Proposal to Fermi National Accelerator Laboratory.

[24] P.E. Karchin et al., IEEE Trans. Nucl. Sci., NS-32, 612 (1985).

[25] N.J. Witchey, Ph.D. thesis, Ohio State University, unpublished (1996).

[26] Introduction to experimental particle physics / R.C. Fernow, Cambridge university press.

[27] J. Raab, Ph.D. thesis, UCSB, unpublished (1987).

[28] D. Bartlett *et al.*, Nucl. Inst. Meth. **A260**, 55-75 (1987).

[29] V.K. Bharadwaj *et al.*, Nucl. Inst. Meth. **228**, 283 (1984).

[30] J.A. Appel *et al.*, Nucl. Inst. Meth. **A243**, 361 (1986).

[31] S. Amato, JRT de Mello Neto, J. de Miranda, C. James, D. Summers, S. Bracker, Nucl. Inst. Meth. **A324** 535 (1993).

[32] R.D. Cousins, V.L. Highland, Nucl. Inst. Meth. **A320**, 331 (1992).

[33] S. MayTal Beck, Ph.D. thesis, Tel-Aviv University, unpublished (1997).

Mexico. University of South Carolina, Columbia, South Carolina. Stanford University, Stanford, California. Tel Aviv University, Tel Aviv, Israel. Tufts University, Medford, Massachusetts. University of Wisconsin, Madison, Wisconsin. Yale University, New Haven, Connecticut.

[10] J.L. Rosner, Phys. Rev. **D33**, 2043 (1986).

[11] T. DeGrand, R.L. Jaffe, K. Johnson, J. Kiskis, Phys. Rev. **D12**, 2060 (1975).

[12] D. Izatt, C. DeTar, M. Stephenson, Nucl. Phys. **B199**, 269 (1982).

[13] S. Zouzou, J.M. Richard, Few Body Systems **16**, 1 (1994).

[14] S. Fleck, C. Gignoux, J.M. Richard and B. Silvestre-Brac, Phys. Lett. **B220**, 616 (1989).

[15] D.O. Riska and N.N. Scoccola, Phys. Lett. **B265**, 188 (1991);
Y. Oh *et al.*, Phys. Rev. **D50** 3350 (1994);
Y. Oh *et al.*, Phys. Lett. **B331** 362 (1994).

[16] Gauge theory of elementary particle physics / Ta-Pei Cheng and Ling-Fong Li, Oxford science publications.

[17] S. Takeuchi, M. Oka, Phys. Lett. **B318**, 1 (1993).

[18] C.B. Dover, U. Heinz, E. Schnedermann, J. Zimanyi,
Phys. Rev. C. **44**, 1636 (1991).

[19] M.A. Moinster, D. Ashery, L.G. Landsberg, H.J. Lipkin,
Z. Phys. A. **356**, 207 (1996).

Bibliography

[1] R.L. Jaffe, Phys. Rev. Lett. **38**, 195 (1977).

[2] A. Chodos, R.L. Jaffe, K. Johnson, C.B. Thorn, and V.F. Weisskopf, Phys. Rev. **D9**, 3471 (1974).

[3] H.J. Lipkin, Phys. Lett. **B195**, 484 (1987).

[4] C. Gignoux *et al.*, Phys. Lett. **B193**, 323 (1987).

[5] M. Bjornberg, Nucl. Phys. **A570**, 625 (1994).

[6] D.O. Riska and N.N. Scoccola, Phys. Lett. **B299**, 338 (1993).

[7] C.K. Chow, Phys. Rev. **D51** 6327 (1995);
C.K. Chow, Phys. Rev. **D53** 5108 (1996).

[8] S. Takeuchi, S. Nussinov, K. Kubodera, Phys. Lett. **B318**, 1 (1993).

[9] E791 collaboration: Centro Brasileiro de Pesquisas Físicas, Rio de Janeiro, Brazil. University of California, Santa Cruz, California. University of Cincinnati, Cincinnati, Ohio. CINVESTAV, Mexico. Fermilab, Batavia, Illinois. Illinois Institute of Technology, Chicago, Illinois. Kansas State University, Manhattan, Kansas. University of Massachusetts, Amherst, Massachusetts. University of Mississippi, Oxford, Mississippi. The Ohio State University, Columbus, Ohio. Princeton University, Princeton, New Jersey. Universidad Autonoma de Puebla,

Chapter 8

Summary

The goal of this work was to search for the pentaquark state via the K^*Kp decay channel, within the framework of E791. The thesis covered the theoretical motivation that led to the search, description of the experimental setup, the analysis methods and the results.

The search objective to reach a sensitivity level of a few percent of that required to detect the D_s meson was achieved. We saw no evidence for pentaquarks decaying to K^*Kp in our data. An upper limit was presented for the ratio of σBR for $P^0_{\bar{c}s} \rightarrow K^*Kp$ and $D_s \rightarrow K^*K$. The upper limit was given as a function of the pentaquark mass and lifetime (see chapter 6).

Our results approach the estimated ratio of production cross-section, assuming similar branching ratios for the two decays: $\frac{BR(P^0_{\bar{c}s} \rightarrow K^*Kp)}{BR(D_s \rightarrow K^*K)} \simeq 1$, and a pentaquark lifetime of 0.4 psec or larger.

A future research based on larger statistics may be able to discover the pentaquark. If the pentaquark existence will be ruled out, it will be an important input to the various models described in chapter 2. However, if the pentaquark will be found, it may improve our understanding of QCD and associated models, opening a path to a new field of hadron spectroscopy.

If we assume that 6 of the 7 events grouped near 2.87 GeV/c^2 in the $\phi\pi p$ mass spectrum are attributed to a pentaquark signal (see fig. 7.1), then we should expect to see 4$\pm$2 events in the K^*Kp channel. The mass spectrum of the K^*Kp channel shows a total of 2 events in the same region. While this is consistent with the expectation of 4$\pm$2, it is also consistent with the expectation of 1 background event in this region. It is important to state that the $\phi\pi p$ paper [34] does not imply in any way that a signal can be seen. The paper concludes: "We see no convincing evidence for pentaquarks decaying to $\phi\pi p$ in our data".

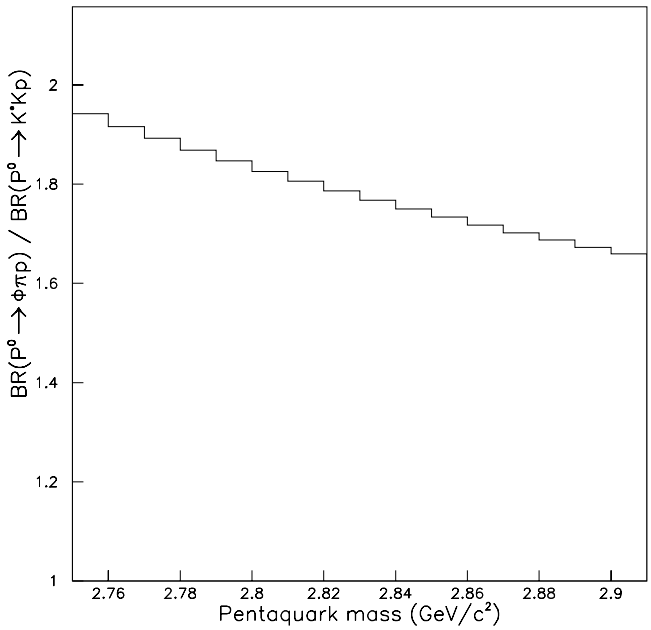

Figure 7.2: The expected ratio $\frac{BR(P^0_{\bar{c}s} \to \phi\pi p)}{BR(P^0_{\bar{c}s} \to K^* K p)}$ as a function of the pentaquark mass.

7.2 Expected ratio of observed events

In order to estimate the expected number of signal events in each channel, there are three factors that should be taken into considerations:

- The theoretical expected ratio $\frac{BR(P^0_{\bar{c}s} \to \phi\pi p)}{BR(P^0_{\bar{c}s} \to K^* K p)}$.
- The detection efficiency with the final selection criteria is 18% larger for the $\phi\pi p$ channel than for the K^*Kp channel [33].
- $\frac{BR(\phi \to K^+K^-)}{BR(K^* \to K^+\pi^-)} = \frac{0.50}{0.67}$ [22].

Hence:

$$\frac{Yield(P^0_{\bar{c}s} \to \phi\pi p)}{Yield(P^0_{\bar{c}s} \to K^* K p)} = \frac{BR(P^0_{\bar{c}s} \to \phi\pi p)}{BR(P^0_{\bar{c}s} \to K^* K p)} \times \frac{BR(\phi \to K^+K^-)}{BR(K^* \to K^+\pi^-)} \times \frac{\epsilon(\phi\pi p)}{\epsilon(K^* K p)} = 1.7 \ to \ 1.4. \tag{7.7}$$

This ratio suggests that the expected number of events observed in the $\phi\pi p$ channel should be ~50% larger than in the K^*Kp channel, for 2.87 GeV/c^2 pentaquark and ~70% for 2.75 GeV/c^2 pentaquark.

- Equal ratio of matrix elements for $P^0_{\bar{c}s}$ and D_s decays were assumed: $\frac{|M^P_{\phi\pi p}|}{|M^P_{K^*Kp}|} \simeq \frac{|M^{D_s}_{\phi\pi}|}{|M^{D_s}_{K^*K}|}$, where the notation M^X_{ABC} represents the matrix element of particle X decaying into the state ABC.

- The matrix elements were assumed to be independent of the momentum; therefore they were taken out from the phase space integral.

Leading to:

$$\frac{BR(P^0_{\bar{c}s} \to \phi\pi p)}{BR(P^0_{\bar{c}s} \to K^*Kp)} \simeq \frac{|M^P_{\phi\pi p}|^2 \times \rho_{\rm ps}(P^0_{\bar{c}s} \to \phi\pi p)}{|M^P_{K^*Kp}|^2 \times \rho_{\rm ps}(P^0_{\bar{c}s} \to K^*Kp)} \simeq \frac{|M^{D_s}_{\phi\pi}|^2 \times \rho_{\rm ps}(P^0_{\bar{c}s} \to \phi\pi p)}{|M^{D_s}_{K^*K}|^2 \times \rho_{\rm ps}(P^0_{\bar{c}s} \to K^*Kp)}. \tag{7.5}$$

The ratio $\frac{|M^{D_s}_{\phi\pi}|^2}{|M^{D_s}_{K^*K}|^2}$ can be derived from the following equation:

$$\frac{BR(D_s \to \phi\pi)}{BR(D_s \to K^*K)} \simeq \frac{|M^{D_s}_{\phi\pi}|^2}{|M^{D_s}_{K^*K}|^2} \cdot \frac{\rho_{\rm ps}(\mathrm{D_S} \to \phi\pi)}{\rho_{\rm ps}(\mathrm{D_S} \to \mathrm{K^*K})} \tag{7.6}$$

where $\frac{BR(D_s \to \phi\pi)}{BR(D_s \to K^*K)} = 1.08 \pm 0.10$ according to experimental data [22].

Calculating the phase space[1] ratio in equation 7.6 yields the matrix element ratio: $\frac{|M^{D_s}_{\phi\pi}|^2}{|M^{D_s}_{K^*K}|^2} \simeq 1.03$. Substituting this value in equation 7.5 and integrating over the three body phase space[2] yields the ratio of $\frac{BR(P^0_{\bar{c}s} \to \phi\pi p)}{BR(P^0_{\bar{c}s} \to K^*Kp)}$.

Figure 7.2 shows the expected ratio $\frac{BR(P^0_{\bar{c}s} \to \phi\pi p)}{BR(P^0_{\bar{c}s} \to K^*Kp)}$ as a function of the pentaquark mass. Comparing between the two decay modes is particularly interesting in the 2.86 GeV/c^2 region where accumulation of events is seen in the $\phi\pi p$ channel (see fig. 7.1). In that region the expected branching ratio is 72% larger for the $\phi\pi p$ channel than for the K^*Kp channel.

[1] Phase space of two-body decays:
The phase space integral is proportional to $\frac{p}{M^2}$, where M is the parent particle mass and p is the momentum of either daughter in the parent particle rest frame. The momentum p is derived from the momentum and energy conservation laws: $p = \sqrt{(M^2 - (m_1 + m_2)^2)(M^2 - (m_1 - m_2)^2)}/2M$.

[2] Phase space of three-body decays:
Three-body phase space is proportional to: $\int_0^{p^{MAX}} \frac{p_3^2 dp_3}{E_3} \cdot$ Phase Space$^{Two-body}$,
where p_3, E_3 are the third daughter momentum and energy respectively (the order of the daughters is not important), and Phase Space$^{Two-body}$ can be calculated as given above.
The upper integration limit is the maximal value that p_3 can retain, without violating the momentum and energy conservation laws: $p^{MAX} = \sqrt{\frac{1}{2}[M^2 - (m_1 + m_2)^2 - m_3^2]}$.

The $P^0_{\bar{c}s} \rightarrow \phi\pi p \rightarrow K^+K^-\pi p$ and $P^0_{\bar{c}s} \rightarrow K^*Kp \rightarrow K^+K^-\pi p$ decay channels originate in the decay of the $\Psi_{D_s^- p}$ component of the pentaquark wave function (see equation 2.19) and are related to the D_s meson decay modes:

$$\begin{array}{lll} D_S \rightarrow & \phi\pi & \rightarrow K^+K^-\pi \\ D_S \rightarrow & K^*K & \rightarrow K^+K^-\pi \end{array} \tag{7.1}$$

There is a considerable difference between the width of the ϕ resonance , $(\phi) = 4.4$ MeV/c^2, and the K^* resonance , $(K^*) = 50.5$ MeV/c^2 [22]. Consequently, the larger width causes the background level in the K^* channel to be an order of magnitude larger than in the ϕ channel (the same argument holds in the pentaquark case). Hence, the K^* channel is more difficult to analyze.

The mass spectrum of the $\phi\pi p$ channel shows an interesting accumulation of events at 2.86 GeV/c^2 (see fig. 7.1); however, no signal evidence can be found in the K^*Kp mass spectrum (see fig. 6.1). In order to compare between the two channels, it is important to estimate the expected ratio of signal events in each channel.

7.1 Estimate of the ratio $\frac{BR(P^0_{\bar{c}s} \rightarrow \phi\pi p)}{BR(P^0_{\bar{c}s} \rightarrow K^*Kp)}$

The partial decay rate $(d, _i)$ of a particle into a n-bodies state is proportional to the squared matrix element $(|M|^2)$ and to the n-bodies phase space element $(d\Phi_n)$:

$$d, _i \propto |M|^2 \cdot d\Phi_n. \tag{7.2}$$

Assuming that the matrix element is independent of the momentum, the above relation can be integrated, yielding:

$$, _i \propto |M|^2 \cdot \rho_{\text{ps}} \tag{7.3}$$

where , $_i$ is the partial width, and ρ_{ps} is the phase space integral.
The branching ratio (BR) of a decay mode is equal to the relative width of the decay mode:

$$BR = \frac{, _i}{\sum , _i}. \tag{7.4}$$

In order to estimate the ratio $\frac{BR(P^0_{\bar{c}s} \rightarrow \phi\pi p)}{BR(P^0_{\bar{c}s} \rightarrow K^*Kp)}$, the following steps were made:

- A mass range for the $P^0_{\bar{c}s}$ was defined.
- The phase space integrals for $P^0_{\bar{c}s} \rightarrow \phi\pi p$ and $P^0_{\bar{c}s} \rightarrow K^*Kp$ were calculated.

Chapter 7

Other pentaquark searches

The only other pentaquark search known so far is via the decay $P^0_{\bar{c}s} \rightarrow \phi\pi p \rightarrow K^+K^-\pi p$ [33]. The $\phi\pi p$ mass spectrum obtained in this search is shown in figure 7.1 (the analysis was done within the framework of E791). The search obtained upper limits for the pentaquark production cross section, relative to the D_s meson production (see equation 6.1), of 0.022, 0.032, 0.025, and 0.046 for pentaquark masses of 2.75 GeV/c^2, 2.79 GeV/c^2, 2.83 GeV/c^2, and 2.87 GeV/c^2, respectively.

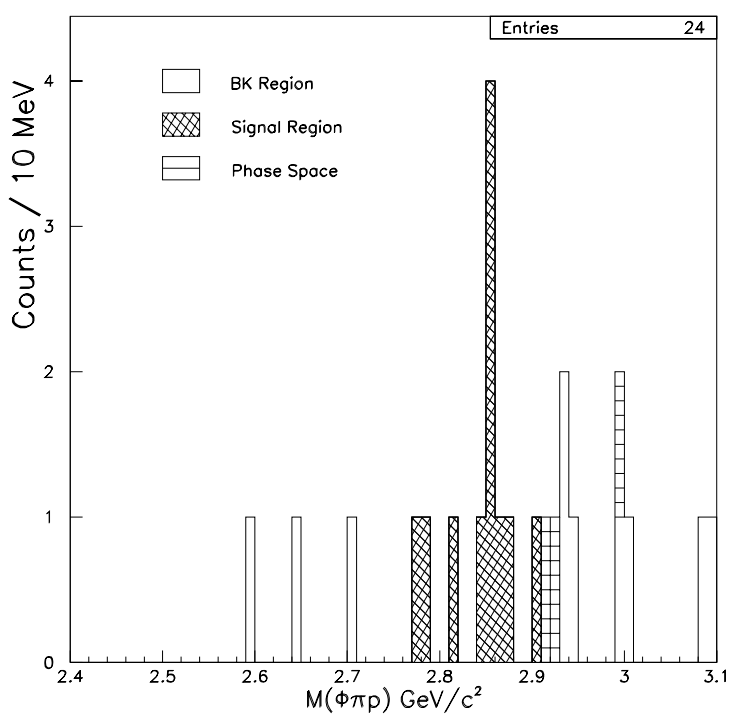

Figure 7.1: The $\phi\pi p$ mass spectrum. The expected region for a pentaquark is cross-hatched. Three phase space events of D_s-p and D^0-p are marked with horizontal lines.

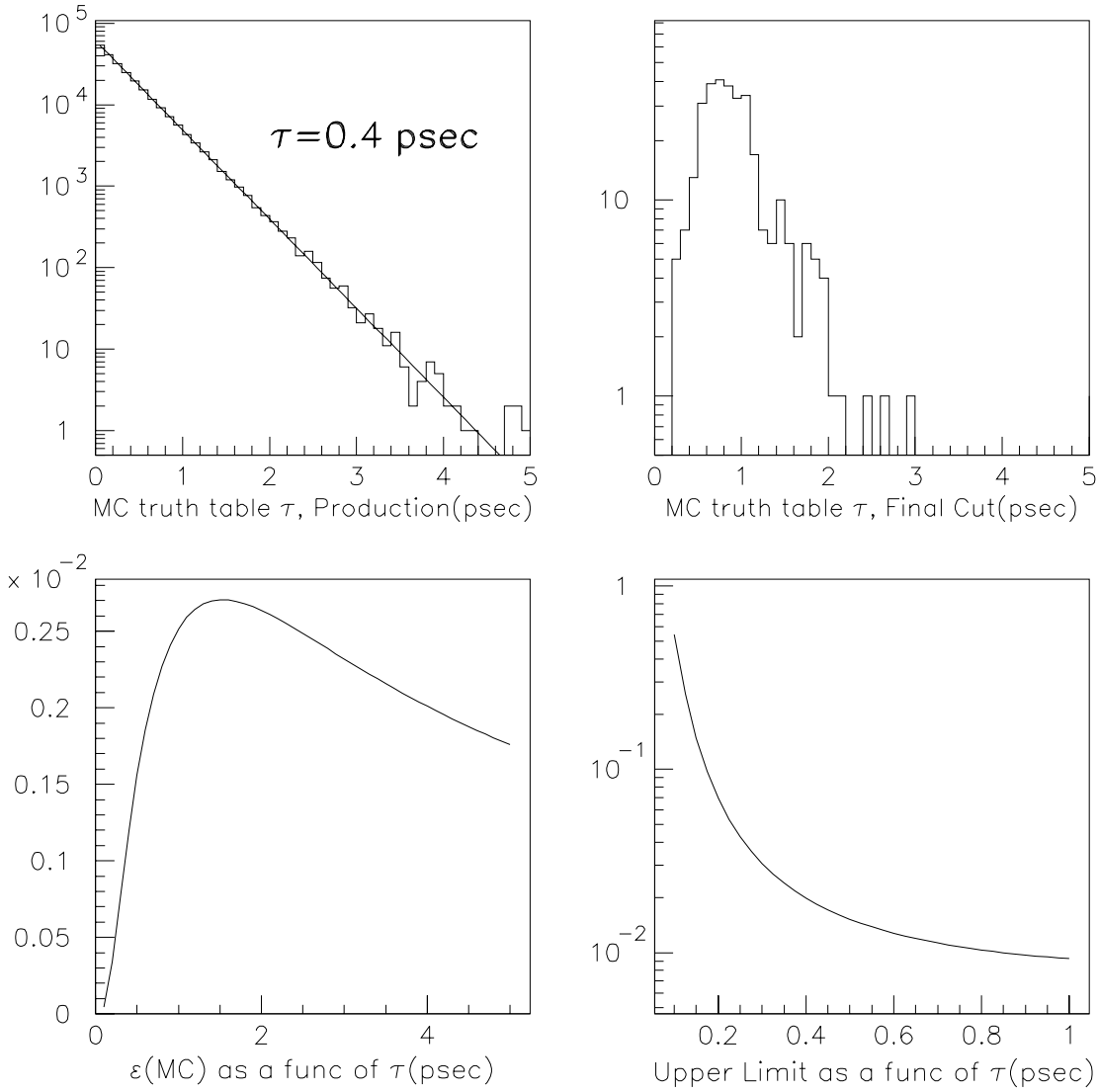

Figure 6.7: Lifetime dependence of the upper limit. The two top histograms show the decay time distribution from pentaquark MC(2.83 GeV/c^2) truth table at production (left), and under final selection criteria (right). The bottom left plot shows the acceptance ϵ(MC) as a function of lifetime, were ϵ(MC) refer to the detection efficiency of pentaquark in the 2.79-2.83 GeV/c^2 mass region. The bottom right plot shows the upper limit of the same mass range as a function of lifetime.

Table 6.2: Upper Limit Results

Mass [GeV/c^2]	Efficiency	Error	Signal	μ	μ'	Upper Limit
2.75-2.79	0.00088	21%	3	5.77	6.1	0.036
2.79-2.83	0.00103	20%	1	3.30	3.5	0.018
2.83-2.87	0.00118	20%	1	3.30	3.5	0.016
2.87-2.91	0.00133	20%	2	4.49	4.7	0.019

The search objective to reach a sensitivity level of a few percent of that required to detect the D_s meson was achieved. The previous charm hadroproduction experiment was E769 which had a signal of 100 D_s (in both $\phi\pi$ and K^*K channels) - the largest D_s sample recorded at that time. E791 data sample was 50 times larger, and enabled the detection of a couple of thousand D_s particles (in both $\phi\pi$ and K^*K channels). In this research the pentaquark selection criteria were applied to the D_s in order to minimize systematic errors. The analysis and optimization procedures were not tuned on the D_s signal, and therfore our D_s signal is not optimal.

6.6 Lifetime dependence

The detection efficiency changes rapidly with the pentaquark (unknown) lifetime. According to theoretical estimates, the pentaquark lifetime might be of the order of $10^{-12} - 10^{-13}$ sec (see section 2.10). MC simulation used $\tau(P^0_{\bar{c}s}) = 0.4$ psec ($\tau(D_s) = 0.47$ psec). Figure 6.7 shows the lifetime dependence of the upper limit. The two top histograms show the decay time from the MC (2.83 GeV/c^2) truth table at production with no selection criteria imposed (left), and under final selection criteria (right). From these two plots, an acceptance function can be extracted. The bottom left plot shows the acceptance ϵ(MC) as a function of lifetime, where ϵ(MC) is the efficiency to detect a pentaquark in the 2.75-2.83 GeV/c^2 mass region. The bottom right plot shows the upper limit of the same mass range as a function of lifetime.

section 6.3. The statistical fluctuations in the observed signal level are included in μ. The systematic errors are described in section 6.4. It is important to state that μ', the corrected upper limit has no error attached.

The final mass spectrum is not flat, nor is the mass dependence of the detection efficiency. The mass resolution for the expected pentaquark signal has a width of 25 MeV/c^2 FWHM. The upper limit was calculated in bins of 40 MeV/c^2 where 93% of the signal is expected to be observed. In order to extract an upper limit from the number of signal entries, the background level should be estimated. For conservative reasons, the background of figure 6.1 was regarded as flat over two bands 2.60-2.75 GeV/c^2, and 2.91-3.06 GeV/c^2. The total of 7 background entries over 300 MeV/c^2 is equivalent to 0.93 events per 40 MeV/c^2 bin.

The two MC(P) samples of 2.75 GeV/c^2 (220K events) and 2.83 GeV/c^2 (260K events) have efficiencies of 0.00080($\pm$7.5%) and 0.00110($\pm$5.9%) respectively, under the final selection criteria.

Table 6.2 summarizes the mass dependent upper limit results. The first column specifies the mass region, the second shows the MC efficiency, deduced and interpolated from the two MC, the third displays the total error (systematic and statistical), and the fourth gives the number of signal entries, taken from the final mass spectrum (see figure 6.1).
On the fifth column appears the 90% confidence level upper limit (μ) on signal entries, as derived from Poisson distribution (see sec. 6.1). The next column shows the value of μ' calculated using equation 6.4. The last column shows the upper limit results, as derived from equation 6.1 (with μ' replacing μ):

$$Upper - Limit = \frac{\mu'/\epsilon(P^0_{\bar{c}s})}{\#D_s/\epsilon(D_s)} = \frac{\mu'/\epsilon(P^0_{\bar{c}s})}{725/0.0038} \tag{6.5}$$

The results are 90% confidence level upper limits on the ratio: $\frac{\sigma \times BR(P^0_{\bar{c}s} \to K^* Kp)}{\sigma \times BR(D_s \to K^* K)}$, where $\sigma \times BR$ is the production cross section (σ) multiplied by the branching ratio (BR). As mentioned at the beginning of this chapter, the ratio is connected to theoretical estimates. Moreover, if $\frac{BR(P^0_{\bar{c}s} \to K^* Kp)}{BR(D_s \to K^* K)} \simeq 1$ then the values in table 6.2 are upper limits on the ratio of production cross section: $\frac{\sigma(P^0_{\bar{c}s})}{\sigma((D_s)}$, for which theoretical predictions were made (see section 2.8).

Table 6.1: Summary of systematic errors.

Parameter	Selection Criterion $P^0_{\bar{c}s}$	Selection Criterion D_s	Systematic Error(%)
SDZ >	10	10	+1.5
ISO >	10μ	10μ	+0.6
DIP <	30μ	30μ	+0.3
DIP(K^*) >	40μ	40μ	−2.0
DCA($K\pi$)<	50μ	50μ	+0.8
PtBal <	0.3 GeV/C	0.3 GeV/C	0.0
RAT <	0.001	0.001	−0.5
RATi/AVER <	3	3	−0.3
RATi <	0.5	0.5	−0.3
$\chi_{(PRI)}$ <	5	5	+0.3
$\chi_{(SEC)}$ <	5	5	−2.2
Č(K1) >	0.14	0.14	−3.8
Č(K2) >	0.14	0.14	+1.8
Č(K1·K2)>	0.05	0.05	+0.8
Č(p) >	0.2	-	−11.
PT2DK >	0.5 [GeV/C]^2	0.5 [GeV/C]^2	−2.1
P(K1),P(K2) >	6 GeV/C	6 GeV/C	+0.7
Seed ≤ 1	+	+	+8.3
Baffle	+	+	+1.9
Miscellaneous	+	+	+2.0
Total			15 %

6.5 Evaluation of the upper limit

The uncertainties should be incorporated into the upper limit. Let us assume an ensemble of experiments conducted under the same conditions, where experiment i results with an upper limit μ_i and an error σ_i. Furthermore, let us assume that the correct upper limit μ, is the average over all μ_i. Thus, it is likely that half of all μ_i will have a value smaller than μ, resulting with an incorrect upper limit (!).
A study carried out by Cousins and Highland [32] concluded that the upper limit should be raised according to the following formula:

$$\mu' = \mu[1 + (\mu - Signal) \times \frac{Error^2}{2}] \tag{6.4}$$

where "$Signal$" is the number of observed events, μ is the upper limit on the "$Signal$" according to Poisson distribution (see section 6.1), and "$Error$" is the combined statistical and systematic error: $Error = \sqrt{Error^2_{statistical} + Error^2_{systematic}}$. The statistical error relates to the normalization channel and MC samples as described in

There are several variables for which the above procedure is not applicable and an alternative way is used:

- SDZ: This variable is correlated with the unknown lifetime of the $P^0_{\bar{c}s}$. Since SDZ is already in error units, the SDZ value was shifted by ± 1, and the larger error between the two options was taken.

- Baffle: The gap effect is not taken into account in the MC; therefore, the systematic error was taken as the whole difference between $\frac{\epsilon(D_s)}{\epsilon(P^0_{\bar{c}s})}$ with and without the Baffle criterion.

- Seed: The Seed variable is not continuous. The systematic error was taken as the whole difference between $\frac{\epsilon(D_s)}{\epsilon(P^0_{\bar{c}s})}$ with and without the Seed selection criterion. Another way to estimate this error is to check the difference between the seed criterion, that permits 1 track difference from the vertex (3 prong for D_s, 4 prong for $P^0_{\bar{c}s}$) and a tighter seed criterion, that demands exactly the same tracks. The two results are roughly the same.

- Proton Čerenkov identification: A proton exists in the pentaquark decay, but not in the D_s decay. A study conducted on protons coming from $\Lambda \to \pi p$ decays, showed that the efficiency to detect protons with Čerenkov probabilities larger than 0.20, is 12% higher in the data than in the MC (for the same momentum bins). An increase of $\epsilon(P^0_{\bar{c}s})$ by 12% causes a decrease of 11% in the upper limit, the proton's Čerenkov systematic error is hence -11%.

- Mis-ID: The misidentifications have no equivalence in the MC, and therefore no systematic error was calculated.

The systematic errors are summarized in table 6.1. Systematic errors have a sign, and should be treated separately since their direction is known. However, most of the significant systematic errors have the same sign (minus). For conservative reasons, we took the quadratic summation of all the systematic errors, regardless of their sign. Consequently the total systematic error grew from 12% to 15%.

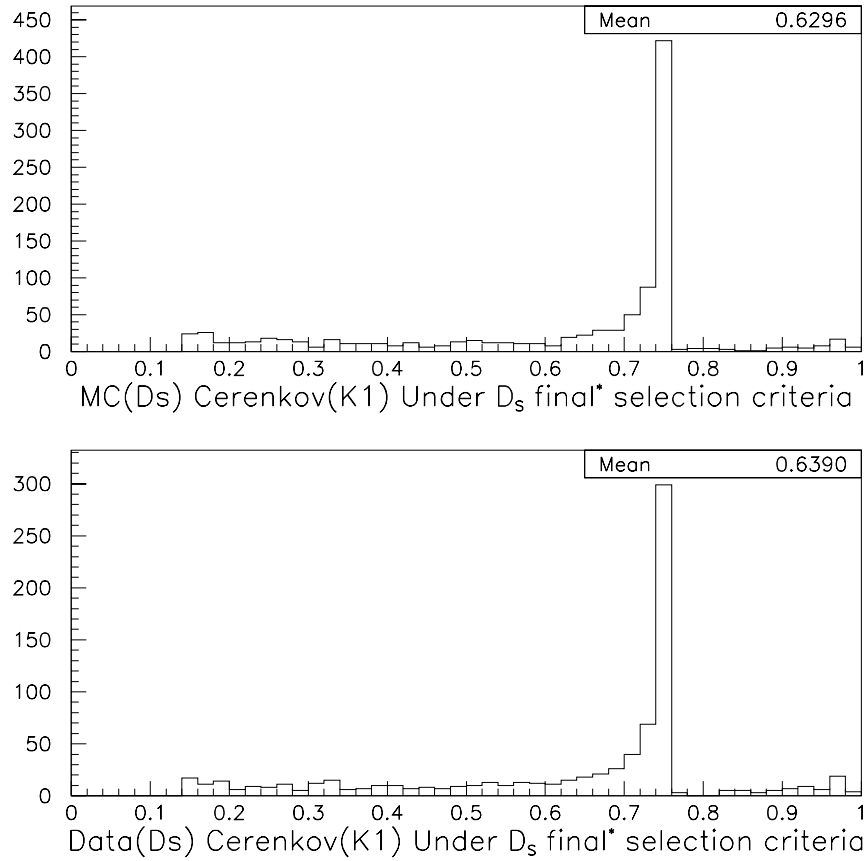

Figure 6.6: Č(K1) (first kaon Čerenkov) systematic error - the difference in the mean value of Č(K1) probability between MC(D_s) and data D_s is +0.009. The corresponding difference between the means of MC($P^0_{\bar{c}s}$) and data(D_s) is -0.018 (not shown). The Č(K1) variable was shifted by these amounts to yield a ratio for $\frac{\epsilon(D_s)_{C(K1)=0.14+0.009}}{\epsilon(P^0_{\bar{c}s})_{C(K1)=0.14-0.018}}$. The difference between this ratio and that using the original values of selection criteria was taken as the systematic error (-3.8%). The Čerenkov probability of the second kaon has similar distribution (the first kaon is the K^* daughter).

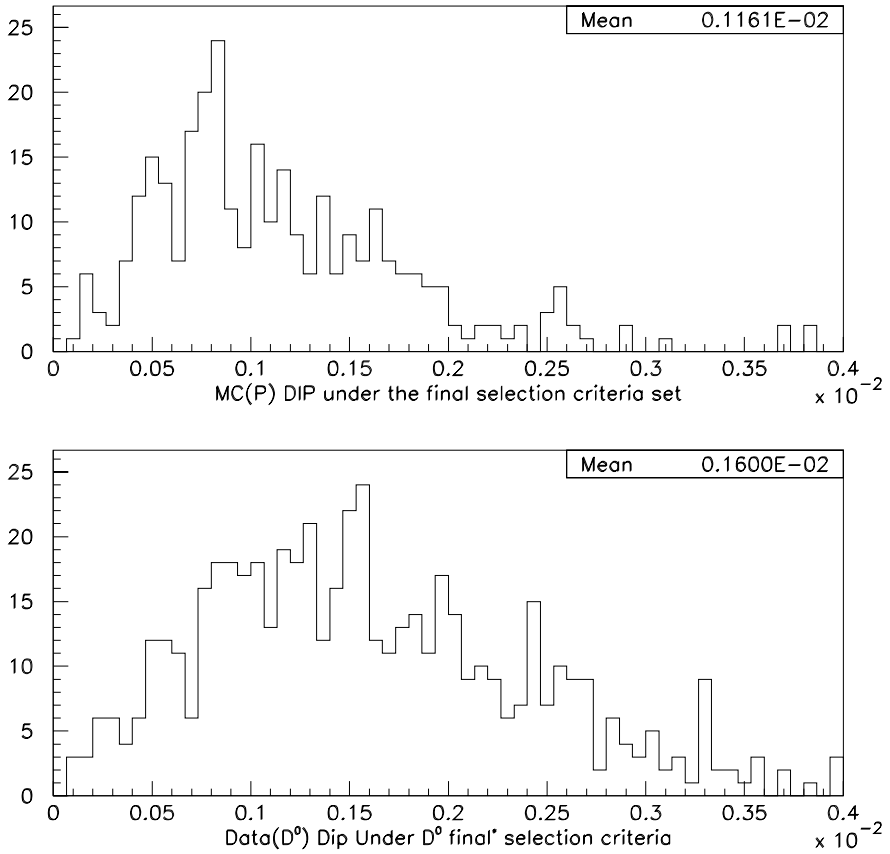

Figure 6.5: DIP systematic error - the difference in the mean value of DIP between MC($P^0_{\bar{c}s}$) and data D^0 is 4.4μ (.00044 cm). The difference between the means of MC(D_s) and data(D_s) is 2.4μ (not shown). The DIP variable was shifted by these amounts to yield a ratio for $\frac{\epsilon(D_s)_{DIP=30-2.4\mu}}{\epsilon(P^0_{\bar{c}s})_{DIP=30-4.4\mu}}$. The difference between this ratio and that using the original values of selection criteria was taken as the systematic error (+0.3%).

- For vertex variables:
  - The Data(D^0) and MC(pentaquark) distributions of each vertex parameter were plotted and the mean value was taken.
  - Each of the pentaquark selection criteria was changed by the difference: Mean[Data(D^0)]–Mean[MC(pentaquark)].
- For Čerenkov and momentum variables:
  - The MC(pentaquark) distributions of each Čerenkov and momentum parameter were plotted and the mean value was taken.
  - Each of the pentaquark selection criteria was changed by the difference: Mean[Data(D_s)]–Mean[MC(pentaquark)].
- The efficiency ratio $\epsilon(D_s)/\epsilon$(pentaquark) was recalculated.
- The change in the ratio was taken as the systematic error for each variable.
- The total systematic error was taken as the quadratic summation of all the systematic errors.

Examples for systematic error estimates can be seen in figures 6.5 (DIP) and 6.6 (Čerenkov). For most of the selection variables, the difference between MC and data distributions is minor.

Figure 6.4 reveals that the D_s signal and the $D^{\pm}$ misidentified signal overlap in a certain region. Moreover, most of the D_s signal is located in the overlap region, making it more difficult to define the shape of the $D^{\pm}$ reflection. Nevertheless, there are no $D^{\pm}$ reflections with a mass below the D_s, thus the misidentified $D^{\pm}$ enhances the background of the D_s histogram (fig. 6.3) in a non-symmetric way. Study of the D_s using maximum likelihood fits, based on the left and right signal shoulders, results in 725^{+88}_{-57} signal events. In order to be conservative, the error is taken as 725 ± 88.

6.3 Statistical errors

The statistical error of the upper limit is derived from the statistical error of the D_s (725 ± 88 particles, see previous section), and the MC statistical errors of MC(D_s) (1524 particles) and MC($P^0_{\bar{c}s}$) (285 particles). The statistical error is taken as the square root of the number of particles that passes the final selection criteria:

$$Statistical\ \ Error(\%) = \sqrt{\left(\frac{88}{725}\right)^2 + \left(\frac{\sqrt{\#MC(D_s)}}{\#MC(D_s)}\right)^2 + \left(\frac{\sqrt{\#MC(P)}}{\#MC(P)}\right)^2} \quad (6.3)$$

The total statistical error is 14%.

6.4 Systematic errors

The systematic errors arise from discrepancies between MC and data. The discrepancies may be different for 3 prong (D_s) and 4 prong ($P^0_{\bar{c}s}$). If the MC and data distributions differ, the MC efficiency has a systematic error, that can shift the ratio $\frac{\epsilon(D_s)}{\epsilon(P^0_{\bar{c}s})}$ and change the upper limit value. Use of this ratio tends to minimize the error.

The following method was used for evaluating the systematic error for each selection criterion:

- The Data(D_s) and MC(D_s) distributions of each analysis parameter were plotted and the mean value was taken.
- Each of the D_s selection criteria was changed by the difference: Mean[Data(D_s)]–Mean[MC(D_s)].

Two signals can be seen in figure 6.3: the D_s meson (on the right) and the $D^{\pm}$ meson (on the left). The decay channel $D^{\pm} \rightarrow K^{*}K$ is Cabibbo suppressed; therefore the $D^{\pm}$ signal is weaker than the D_s signal although the D_s has lower production cross section.

The background levels on both sides of the D_s signal are significantly different - 12 (28) events per 5 MeV/c^2 bin in the left (right) shoulder. The reason for the non-symmetric background level is a reflection of misidentified $D^{\pm} \rightarrow K\pi\pi$ decays. Figure 6.4 is a two dimensional plot of $K\pi\pi$ versus $KK\pi$ invariant masses. The vertical axis is calculated by assigning to one kaon track a π mass (the kaon with charge opposite to the π).

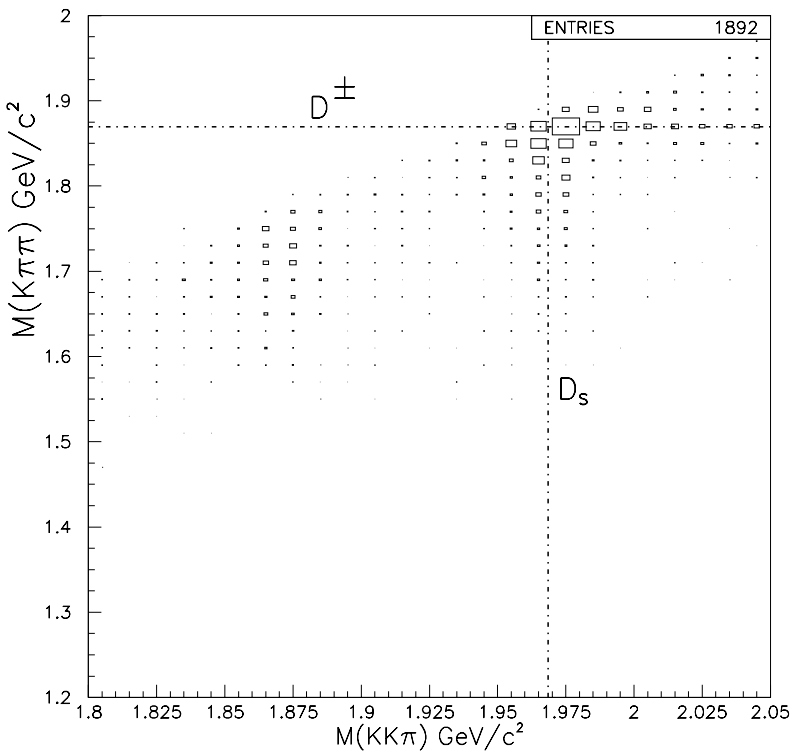

Figure 6.4: Two dimensional plot of $K\pi\pi$ versus $KK\pi$ invariant masses. The $K\pi\pi$ invariant mass reveals a misidentified $D^{\pm} \rightarrow K\pi\pi$ signal. This histogram has exactly the same entries as the previous one.

6.2 The D_s signal

Figure 6.3 shows the K^*K mass spectrum from data under the final selection criteria (see table 5.1). However, since the decay channel $D_s \rightarrow K^*K$ has no proton, the proton Čerenkov and momentum criteria were not considered.
The term $\#D_s/\epsilon(D_s)$ of equation 6.1 remains unchanged (within errors) under all three sets of selection criteria as appear in table 5.1, indicating that the MC(D_s) describes well the data(D_s).

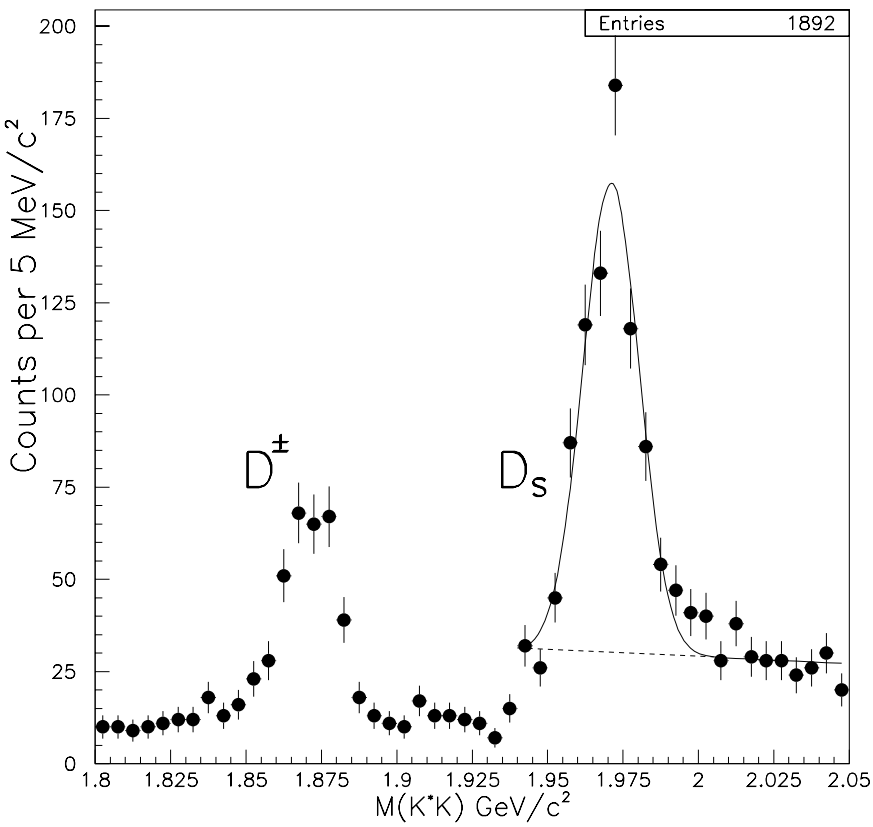

Figure 6.3: The K^*K mass spectrum from data under the final selection criteria. Two signals can be seen: D_s meson (right) and $D^{\pm}$ meson (left). The background levels on both sides of the D_s signal are not symmetric (see discussion in sec. 6.2).

6.1 Upper limit for Poisson processes

If we observe n_0 events in a Poisson process which has two components, signal (unknown) and background (μ_B), then the upper limit on the number of signal events (N), with a confidence level ϵ (0.90 in our case) is given by [22]:

$$1 - \epsilon = 1 - \frac{e^{-(\mu_B+N)} \sum_{n=0}^{n_0} \frac{(\mu_B+N)^n}{n!}}{e^{-\mu_B} \sum_{n=0}^{n_0} \frac{\mu_B^n}{n!}} \tag{6.2}$$

Figure 6.2 shows the 90% confidence level upper limit on the number of signal events as derived from equation 6.2.

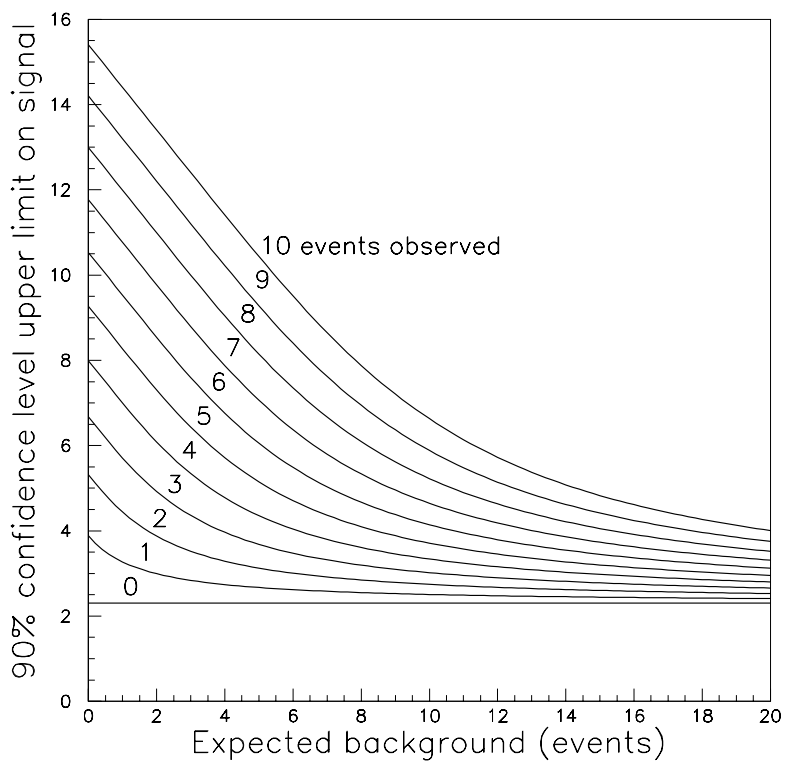

Figure 6.2: A 90% confidence level upper limit on the number of signal events as a function of the expected number of background events. For more details see [22].

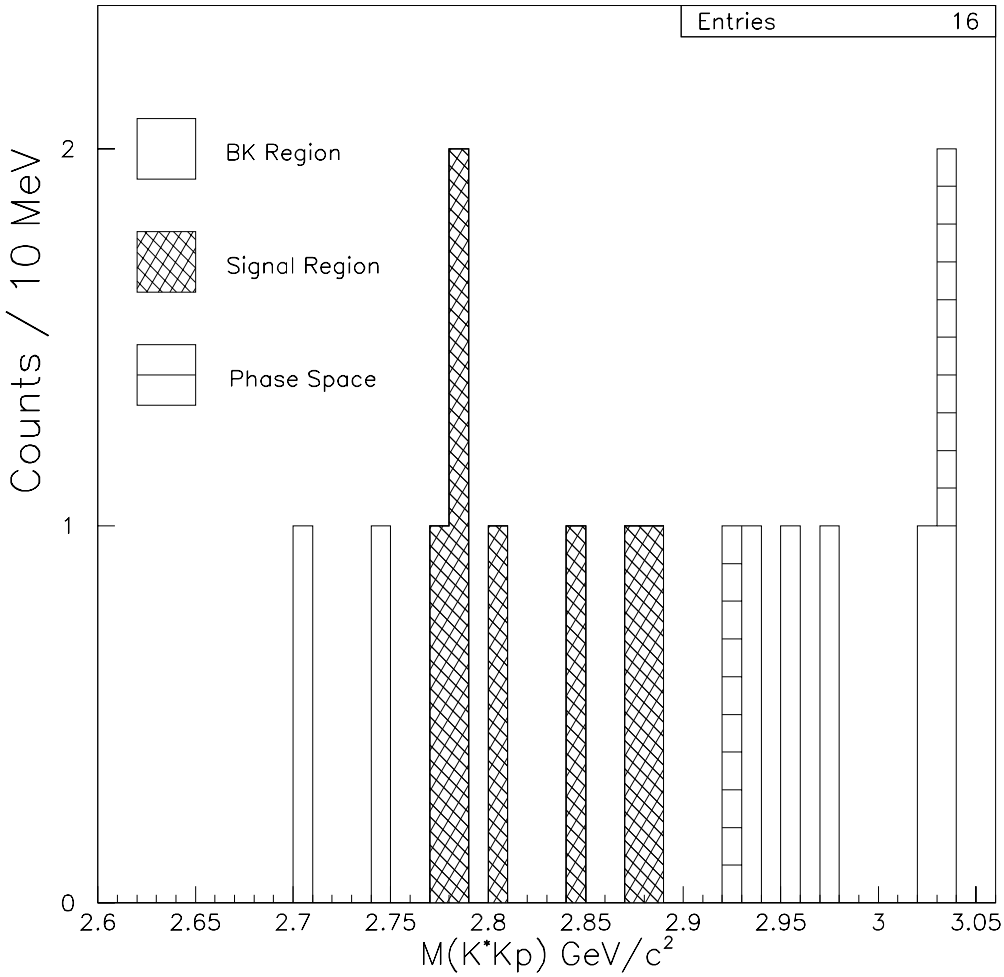

Figure 6.1: The K^*Kp mass spectrum from data under the final selection criteria. The signal region is cross-hatched. Two phase space events of D_s-p and $D^{\pm}$-p are marked with horizontal lines.

Using the ratio of equation 6.1 helps to minimize systematic errors that usually have the same sign and similar magnitudes for both particles. Moreover, the ratio is better connected to theoretical estimates (see section 2.8).

The final selection criteria are the basis for deriving the upper limit. In our study the pentaquark efficiency was found to be 0.0011 ($\pm 7 \times 10^{-5}$), the D_s efficiency 0.0038 ($\pm 1 \times 10^{-4}$), and the number of observed D_s 725^{+88}_{-57} (see section 6.2).

Chapter 6

Results

This chapter presents the thesis results. Figure 6.1 shows the $\bar{K}^*Kp$ mass spectrum from data under the final selection criteria (see table 5.1). The signal region is cross-hatched. Two events above threshold have a K^*K invariant mass consistent with the D_s and $D^{\pm}$ masses. Since both D mesons have a K^*K decay channel, these events are referred to as phase space events of D_s-p and $D^{\pm}$-p (marked with horizontal lines). These events lie above the pentaquark threshold (D_s-p at 2.907 GeV/c^2) and were excluded for background level estimate in order to be more conservative in the upper limit evaluation (see section 6.5).

The pentaquark decay to K^*Kp and the D_s decay to K^*K are closely related. Since no clear signal can be seen in figure 6.1, an upper limit is calculated on the ratio:

$$Upper - Limit = \frac{\mu/\epsilon(P^0_{\bar{c}s})}{\#D_s/\epsilon(D_s)} \tag{6.1}$$

where:

μ	is the 90% confidence level upper limit on the number of signal events, as derived using Poisson statistics (see section 6.1).
$\#D_s$	is the number of D_s events reconstructed from the data.
$\epsilon(P^0_{\bar{c}s})$, $\epsilon(D_s)$	are the efficiencies of the $P^0_{\bar{c}s}$ and D_s, respectively.

The efficiencies $\epsilon(P^0_{\bar{c}s})$ and $\epsilon(D_s)$ are estimated by dividing the number of MC events that pass the selection criteria by the number of generated MC events. Since the MC has discrepancies, systematic errors were estimated as well (see section 6.4).

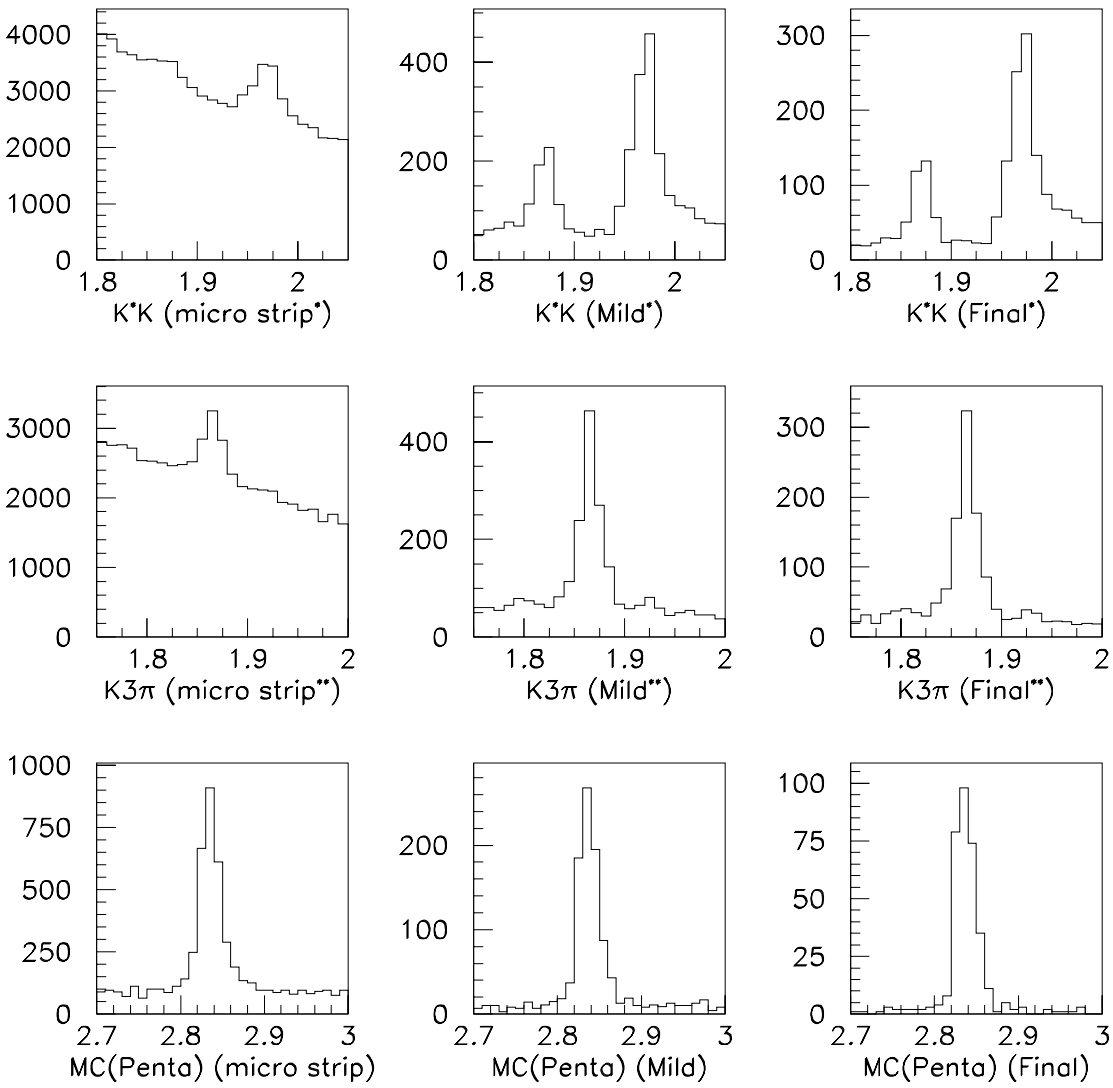

Figure 5.8: The signals that were used in the optimization procedure: The data D_s at the top row, the data D^0 in the middle row and the MC(pentaquark) at the bottom row. The micro strip cuts are applied in the left column, the mild set is applied in the center column, and the final set is applied in the right column. The D_s selection criteria do not include proton Čerenkov and momentum criteria (marked by '$*$'). The D^0 selection criteria (marked by '$**$') do not include proton and second kaon Čerenkov and momentum criteria. Moreover, the D^0 Pt2DK selection criterion has a value of 0.3 GeV^2/c^2 (instead of 0.4-0.5 GeV^2/c^2) due to its low Q value (the original values eliminate most of the D^0 signal).

At the bottom of table 5.1, appears the sensitivity (Pentaquark(MC)/$\sqrt{Background}$), as calculated under each set. The objective of the selection criteria is to reach the highest sensitivity. The price is a reduction in the efficiency by an order of magnitude.

In figure 5.8 appear the data D_s signal (top row), the data D^0 (center row) and the MC(pentaquark) at the bottom row. The micro strip set is applied in the left column, the mild set in the center column, and the final set is applied in the right column.

The differences in the decay channels of $P^0_{\bar{c}s} \rightarrow KK\pi p$, $D_s \rightarrow KK\pi$ and $D^0 \rightarrow K\pi\pi\pi$ required some adjustment in the selection criteria sets:

- The D_s criteria do not include the proton Čerenkov and momentum criteria (marked by '$*$').
- The D^0 criteria (marked by '$**$') do not include proton and second kaon Čerenkov and momentum criteria. Moreover, the D^0 Pt2DK selection criterion has a value of 0.3 GeV^2/c^2 (instead of 0.4-0.5 GeV^2/c^2) due to its lower Q value (the original values eliminate most of the D^0 signal).

5.8 Table of selection criteria

Table 5.1: Table of selection criteria.

Parameters	Sub Strip	Micro Strip	Mild Set	Final Set
SDZ >	4	8	10	10
ISO >	-	-	10μ	10μ
DIP <	80μ	60μ	40μ	30μ
DIP(K^*) >	-	-	-	40μ
DCA($K\pi$)<	50μ	50μ	50μ	50μ
PtBal <	-	-	0.5 GeV/c	0.3 GeV/c
RAT <	0.01	0.01	0.001	0.001
RATi/AVER <	-	-	3	3
RATi <	-	-	0.5	0.5
$\chi_{(PRI)}$ <	5	5	5	5
$\chi_{(SEC)}$ <	5	5	5	5
Č(K1) >	0.14	0.14	0.14	0.14
Č(K2) >	0.12	0.12	0.14	0.14
Č(K1 · K2)>	0.05	0.05	0.05	0.05
Č(p) >	0.038	0.038	0.038	0.2
PT2DK >	-	-	0.4 [GeV/c]^2	0.5 [GeV/c]^2
P(K1),P(K2) >	-	-	6 GeV/c	6 GeV/c
P(proton)	-	-	-	21-75 GeV/c
Seed ≤ 1	-	-	-	+
Mis-ID, Baffle	-	-	-	+
Miscellaneous	-	-	+	+
Efficiency	0.0113	0.0091	0.0029	0.00110
Efficiency Error	$\pm$0.0002	$\pm$0.0002	$\pm$0.0001	$\pm$0.00007
Sensitivity	5.3 $\pm$ 0.1	7.1 $\pm$ 0.1	25 $\pm$ 1	100 $\pm$ 18

The definitions of all the parameters are given in sections 5.4 through 5.7. The mark '>' ('<') in the left column means that candidates with parameter value larger (smaller) than the ones given in the table were selected. Č(K1) and Č(K2) stand for the kaon Čerenkov probability of the first kaon (K^* daughter) and second kaon, respectively. Č(K1·K2) is the product of Č(K1) and Č(K2). Č(p) is the proton Čerenkov probability. P(K1), P(K2) and P(proton) represent the momenta of the particles.

The Seed$\leq$ 1 criterion is explained in section 5.4.10. The miscellaneous criterion stands for all selection criteria described in sections 5.6.1 - 5.6.2. The '+' ('$-$') sign means that the selection criterion was (was not) applied.

The misidentified signal forms usually a flat distribution in the pentaquark mass spectrum. However, it may create a reflection - where the misidentified particle forms a signal shape in the pentaquark mass spectrum. This poses a hazard to a new particle analysis as one must be sure that a signal has not originated from reflections. Figure 5.7 shows the K, K, π, p mass distribution of the rejected misidentified events, under the mild set of selection criteria. The distribution is rather flat, meaning that rejecting those events does not create peaks in the pentaquark mass spectrum.

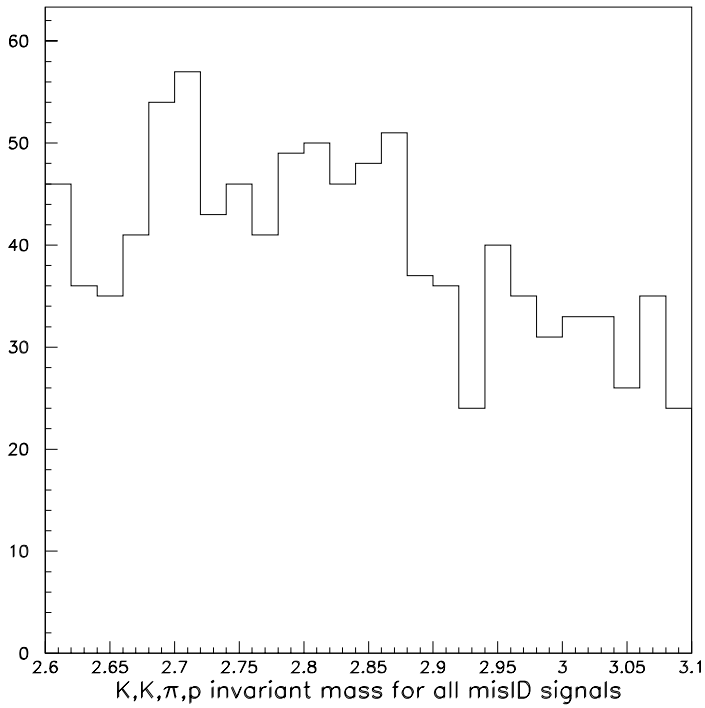

Figure 5.7: $KK\pi p$ mass distribution of events that were rejected due to misidentification, plotted under the mild set of selection criteria.

The Čerenkov counters were not perfect and such misidentification could happen. The method we used to search for the misidentified signals was to take the data sample and assume different combinations of particles. Then we calculated the invariant mass, and received the misidentified spectrum.

An extensive misidentification study was done on many possible background sources: Two prong such as $\Lambda \to p\pi$, $\phi \to KK$, three prong such as $D^+ \to K\pi\pi$, $D_s \to KK\pi$, and four prong such as $D^0 \to K\pi\pi\pi$, $D^0 \to \pi\pi\pi\pi$.
The conclusions were that the decay products of $D^0 \to K\pi\pi\pi$ could be misidentified as $KK\pi p$, and the decay products of $\phi \to KK$ with two additional tracks (originating in the primary vertex) could be misidentified also as $P^0_{\bar{c}s} \to KK\pi p$. In figure 5.6 one can see a misidentified D^0 signal (top) and a misidentified ϕ signal (bottom), both under the mild selection criteria (see table 5.1). These two Misidentified sources were rejected from the final sample (The D^0 mass window was 1.840-1.890 GeV/c^2, while the ϕ mass window was 1.009-1.029 GeV/c^2).

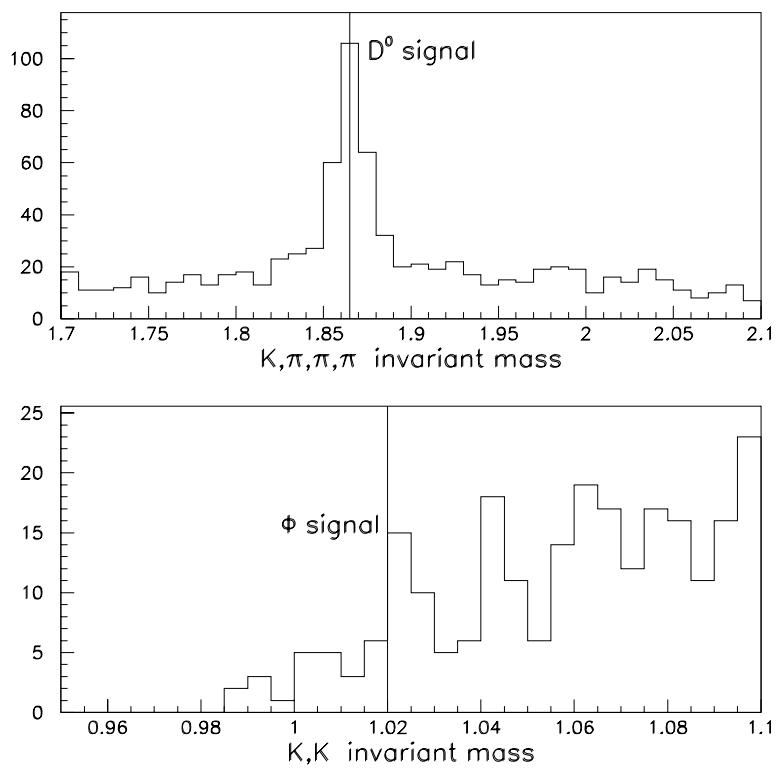

Figure 5.6: Misidentified signals of $D^0 \to K\pi\pi\pi$ (top), and $\phi \to KK$ (bottom), both under the mild selection criteria set. The vertical lines indicates the exact masses of the D^0,ϕ particles.

speaking, the lower the amount of Čerenkov light associated with a track, the higher the probability that the track is produced by a heavy mass particle such as a kaon or a proton (see table 3.2). Any secondary vertex with one of its proton/kaon tracks passing through the mirror's gap was rejected.

5.6.4 Ghost tracks

The reconstruction routine used detector hits to generate tracks (see section 4.1). Sometimes, due to noise in the SMD detectors, two tracks were based on hits originating from a single particle ("Ghost" tracks). In such cases, the angle between the two tracks was close to zero. Tracks with nearly identical slopes were rejected. The distribution of the angle between any two tracks, $\sin(\theta)$, was generally monotonic except for the sharp peak at zero ($\theta < 0.0001$) which reflects the ghost tracks (see fig. 5.5). Pairs of tracks in this region were rejected.

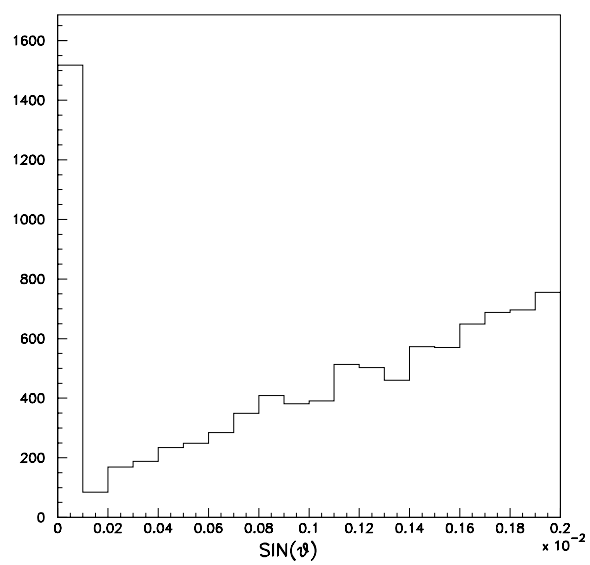

Figure 5.5: $\mathrm{Sin}(\theta)$ between pairs of secondary vertex tracks. The enhancement in the first bin ($\mathrm{Sin}(\theta) < 0.0001$) is due to "Ghost" tracks.

5.7 Misidentification of particles

The motivation of the misidentification study was to identify background that comes from decay of a known particle, and its daughters were misidentified as K, K, π, p.

5.6 Additional selection criteria

Several more selection criteria were used:

5.6.1 Tracks

- All tracks with $\chi^2 > 5$ per degree of freedom were not considered as good enough for vertexing.
- All tracks were required to pass at least the first two drift chamber stations (see section 3.1.3) for better momentum resolution.

5.6.2 Vertices

- The location of the primary and secondary vertices was limited to be upstream of the interaction counter, located 2 cm downstream of the last target foil.
- A secondary vertex was rejected if it was located within 2.5 sigma from a target edge, where sigma is the distance of the secondary vertex from the nearest target edge divided by the error on the vertex z location: $Sigma = \frac{Z_{Secondary} - Z_{Target}}{\sigma_{sec}}$. This criterion rejected secondary interactions in which a track from the primary vertex hits a target foil downstream and produces new tracks that might appear as a secondary vertex.
- A secondary vertex was rejected if one of its tracks was associated with another secondary vertex (a track is allowed to appear in more then one secondary vertices, see section 4.1) located within a target foil.
  This criterion rejects another sort of secondary interactions, where one track that originated in a secondary interaction, is joined to the candidate decay vertex.

5.6.3 The Čerenkov mirror gap (baffle)

A horizontal screen (baffle) between the upper and lower mirror arrays was placed to protect the Čerenkov phototubes from photoproduced e^+e^- pairs during experiment E691 that used an earlier version of the E791 spectrometer. In E769 and E791 the screen was not necessary, (only needed in the beam region) but was not removed.
For tracks heading into the midplane region (defined by $-0.0025 < dy/dz < 0.0000$; where dy/dz is the slope of the track in y direction), the Čerenkov phototubes received no light due to the baffle, resulting in high proton and kaon probabilities. Generally

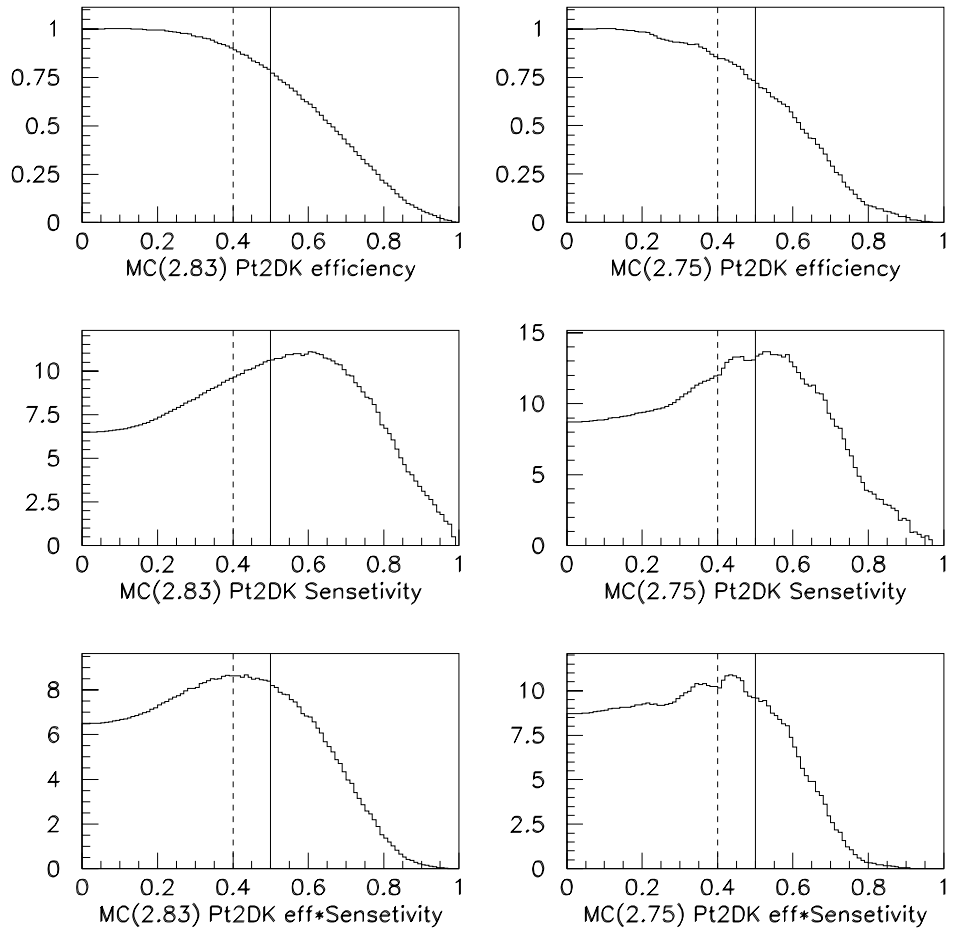

Figure 5.4: Optimization of the selection criterion for the Pt2DK parameter. From top to bottom appear the Pt2DK efficiency, sensitivity and the product of efficiency and sensitivity. Pt2DK taken from the pentaquark(MC) sample of 2.83 GeV/c^2 appear on the left, while Pt2DK taken from the pentaquark(MC) sample of 2.75 GeV/c^2 appear on the right. The dashed vertical line indicates the Pt2DK selection criterion of the mild set, placed at the peak of the product of efficiency and sensitivity. The solid line indicates the Pt2DK selection criterion chosen for the final set, placed at the peak of sensitivity for pentaquark of the mass of 2.75 GeV/c^2. All histograms are plotted under the micro strip set of selection criteria.

5.5.3 Optimization example: The Pt2DK parameter

The Pt2DK distribution can be taken only from pentaquark(MC) as this parameter depends on the specific Q value of the decay channel (see section 5.4.6). MC and data Pt2DK distributions of D_s and D^0 for several decay modes were checked and found to be practically identical. The Pt2DK is a kinematic parameter, and the MC predicts its distributions accurately.

The Q value directly depends on the unknown mass of the pentaquark and its selection criterion should be set to fit pentaquarks of any mass in the expected mass region. Therefore, two pentaquark(MC) samples of different masses were used in the optimization process.

Optimization of the selection criterion applied on the Pt2DK parameter is shown in figure 5.4. From top to bottom appear the Pt2DK efficiency, sensitivity and the product of efficiency and sensitivity. Pt2DK taken from the pentaquark(MC) sample of 2.83 GeV/c^2 appear on the left side, while Pt2DK taken from the pentaquark(MC) sample of 2.75 GeV/c^2 appear on the right side.
The dashed vertical line in figure 5.4 indicates the Pt2DK selection criterion chosen for the mild set (see table 5.1), placed at the peak of the product of efficiency and sensitivity (0.4 GeV^2/c^2). The solid line indicates the Pt2DK selection criterion chosen for the final set (see table 5.1), placed at the peak of sensitivity for pentaquark of the mass of 2.75 GeV/c^2 (0.5 GeV^2/c^2).

The selection criteria for the other parameters were chosen in a similar way to that described in this section and its previous ones. The only parameters for which this procedure was not applicable were are described in sections 5.6 through 5.7. The Seed parameter has discrete values. Its optimization was done using efficiency, sensitivity and their product for discrete values and following the same logic as for the other parameters.

5.5.2 Optimization example: The kaon Čerenkov parameter

Optimization of the selection criterion applied to the kaon Čerenkov parameter is shown in figure 5.3. Efficiency, sensitivity distributions and their product from pentaquark(MC) appear on the left while distributions from D_s(Data) appear on the right. From top to bottom appear the kaon Čerenkov efficiency, sensitivity and the product of efficiency and sensitivity.

The kaon Čerenkov sensitivity plots are flat up to 0.7 where they decrease. Therefore the kaon Čerenkov criterion remain unchanged, in its micro strip value.

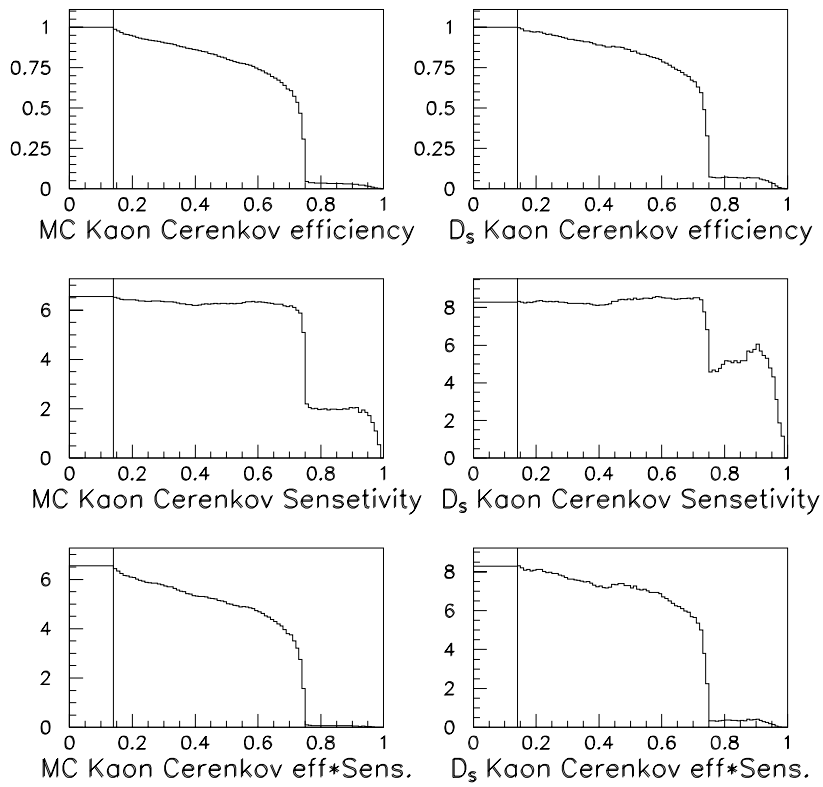

Figure 5.3: Optimization of the selection criterion for the kaon Čerenkov parameter. Kaon Čerenkov taken from pentaquark(MC) appear on the left while kaon Čerenkov taken from D_s(Data) appear on the right. From top to bottom appear the kaon Čerenkov efficiency, sensitivity and the product of efficiency and sensitivity. The solid vertical line indicates the kaon Čerenkov selection criterion chosen for the final set, which remains unchanged from its micro strip level at 0.14. All histograms are plotted under the micro strip set of selection criteria.

all parameters showed the same characteristic distributions as before, reflecting weak correlations between the various parameters. At this stage the final set of selection criteria was chosen by setting all parameters at the peak of sensitivity. The solid vertical line placed at 0.003 cm in figure 5.2 indicates the final DIP selection criterion. The iterative procedure helped verify that the selection criteria chosen are stable.

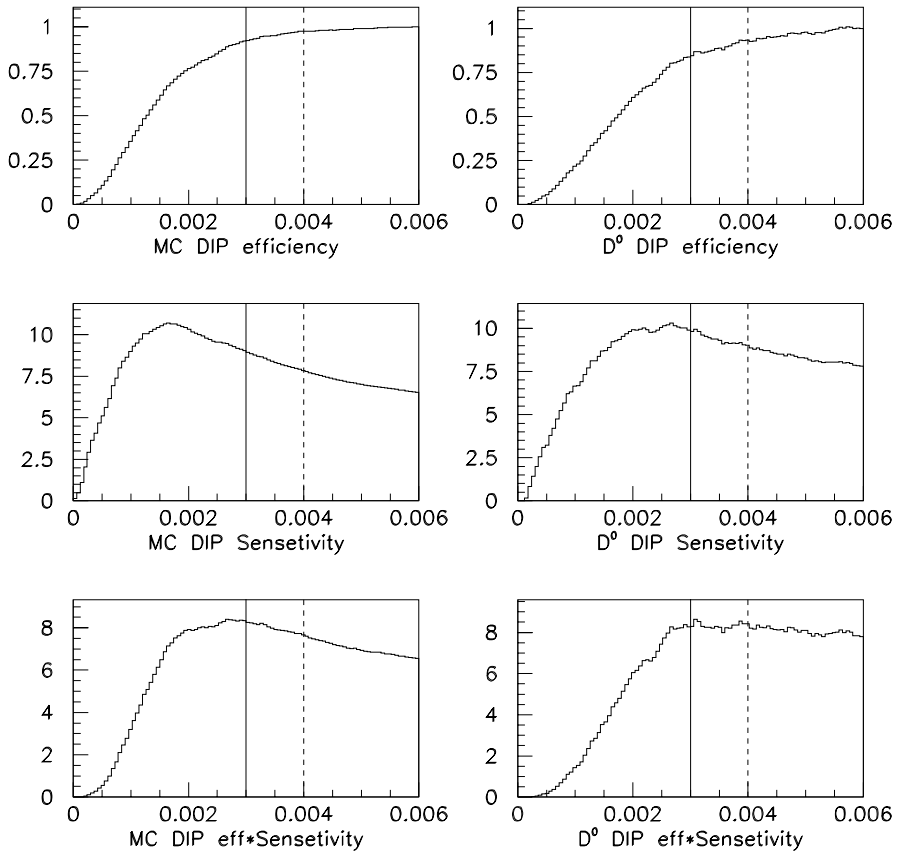

Figure 5.2: Optimization of the selection criterion for the DIP parameter. DIP taken from pentaquark(MC) appear on the left while DIP taken from D^0(Data) appear on the right. From top to bottom appear the DIP efficiency, sensitivity and the product of efficiency and sensitivity. The dashed vertical line indicates the DIP selection criterion chosen for the mild set of selection criteria, placed at the peak of the product of efficiency and sensitivity (0.004 cm). The solid line indicates the DIP selection criterion chosen for the final set of selection criteria, placed at the peak of sensitivity (0.003 cm). All histograms are plotted under the micro strip set of selection criteria.

distributions. The sensitivity was calculated as a function of a cut applied on a vertex parameter, for both data D^0 and pentaquark(MC) to check if and where the MC does not follow the data well. For the D^0 sensitivity the signal was taken from the data D^0 and for the pentaquark sensitivity the signal was taken from the pentaquark(MC). The background was taken in both cases from the pentaquark data outside the expected signal region (see example in section 5.5.1).

- The MC was trusted for some kinematic parameters, such as PT2DK (see section 5.4.6).

The goal was to find optimal criteria that could separate the signal from the background, achieving high sensitivity with reasonable efficiency.

5.5.1 Optimization example: The DIP parameter

Optimization of the selection criterion applied to the DIP parameter is shown in figure 5.2. From top to bottom appear the DIP efficiency, sensitivity and the product of efficiency and sensitivity. The efficiency is defined as the ratio of the number of signal events that pass the selection criterion, and the number of signal events under the micro strip set (see table 5.1). They are plotted as a function of the DIP selection criterion. Thus, the efficiency starts from 1 and reach 0 for extremely tight values of the selection criterion. DIP taken from pentaquark(MC) appear on the left, while DIP taken from D^0(Data) appear on the right.

The DIP is a good example for a MC discrepancy - MC shows that the sensitivity peaks at 0.002 cm, while the D^0 data sensitivity peak is located near 0.003 cm (see figure 5.2). In cases where MC predictions differ from data signals, it was believed that the MC is inaccurate, and the selection criterion was chosen according to the data signal.

In order to study correlations between the selection parameters, two iterations of the optimization procedure were made. In the first iteration all parameters were plotted under the sub-strip set of selection criteria (see selection criteria sets in table 5.1), and a mild set of selection criteria was chosen by setting all parameters at the peak of efficiency times sensitivity. The dashed vertical line placed at 0.004 cm in figure 5.2 indicates the DIP selection criterion, under the mild set. In the second iteration, all parameters were plotted under the mild set of selection criteria. Nearly

The Seed parameter counts the number of tracks not common to the secondary vertex found by the analyzer and by the reconstruction routine. For example, the Seed≤ 1 criterion selects only those analyzer secondary vertices that differ from the vertexer secondary by no more than one track.

5.5 Determination of selection criteria

In order to avoid bias, we developed a semi-automatic method to optimize the selection criteria. The determination of optimal and unbiased selection criteria was done in the following way:

- The data signal region(2.75-2.91 GeV/c^2) was masked.
- The pentaquark mass signal was simulated by MC, while the background was taken from the data outside of the expected signal region: 2.60-2.75 GeV/c^2 and 2.91-3.06 GeV/c^2. A selection criterion was chosen in order to reach the best sensitivity: Signal(MC)/$\sqrt{Background}$, which is the optimal way to distinguish between signal and background (i.e. to reach the largest significance of the signal). The technique is described in the following sub-sections.
- The MC had some discrepancies that required a comparison of MC predictions and data signals:
  - The Čerenkov MC predictions for kaons were checked using D_s data signal. The D_s has the same daughters as the pentaquark, except for the proton. Therefore, the Čerenkov spectra of K, K, π should have similar distributions (see example in section 5.5.2).
    The sensitivity was calculated as a function of a cut applied on the kaon Čerenkov parameter, for both data D_s and pentaquark MC to check if and where the MC does not follow the data well. For the D_s sensitivity the signal was taken from the D_s data, and for the pentaquark sensitivity the signal was taken from the pentaquark(MC). The background was taken in both cases from the pentaquark data outside the expected signal region.
  - The vertex MC predictions were checked using D^0 data signal.
    The $D^0 \rightarrow K\pi\pi\pi$ is a four prong vertex, with a relatively strong and clean signal. It's lifetime is $0.42 \cdot 10^{-12}$ sec, similar to that used in the MC, enabled the use of the same SDZ values as used for the pentaquark. Vertex parameters of the D^0 data and pentaquark(MC) signals should have similar

scalars that indicate the kinematics of the decay process. Pt balance is correlated with DIP, both checking different aspects of the secondary momentum with respect to the primary position.

5.4.8 RAT, RATi, RATi/AVER

RAT measures the likelihood that track(s) belong to the secondary or to the primary vertex. Several variations of the same principle were used. RATi is the ratio between the impact parameter of a track with respect to the secondary and primary vertices

$$RATi = \frac{IP_{sec}}{IP_{pri}} \tag{5.3}$$

where IP_{pri} (IP_{sec}) is the impact parameter of track i with respect to the primary (secondary) vertex. Tracks having low RATi are more likely to originate from the secondary vertex then from the primary vertex.
RAT is the product of RATi for all the secondary vertex tracks:

$$RAT = \prod_{i=1}^{4} RATi. \tag{5.4}$$

The last combination is RATi/AVER, which is RATi divided by the averaged RATi. The motivation to use RATi/AVER came from cases where one extremely low RATi leads to a low RAT which is misleading. RATi/AVER is normalized by the averaged RATi, and may be more sensitive in such cases.

5.4.9 Vertex χ^2

The vertex χ^2/Degree-of-Freedom (see section 4.1) was used in order to rule out vertices with large errors. Vertices with large χ^2 are poorly defined, reflecting on other selection criteria based on the vertex location, such as DIP, RAT, ISO, etc. (see fig. 5.1).

5.4.10 Seed

The vertexing algorithm used by the reconstruction routine was based on tracks geometry (see section 4.1). In order to increase the efficiency, the analyzer algorithm searched for any four tracks that satisfy the micro strip set of selection criteria. However, the analyzer algorithm had a higher background level. It was found that combining the two methods (analyzer and vertexer algorithms) improves the sensitivity of any method by itself.

5.4.3 DIP

The parent momentum is the vector sum of all secondary tracks momenta. DIP is defined as the distance between the primary vertex and the projection of the parent momentum back to the z-position of the primary vertex (see fig. 5.1). DIP measures how well the reconstructed parent particle momentum points back to the primary vertex.

5.4.4 DIP(K^*)

DIP(K^*) is calculated in the same manner as the DIP variable except that the parent momentum is extracted exclusively from the K^* daughter particles K,π.
Studies done on D_s data, D_s MC, and pentaquark MC showed that K^*s coming from D_s and $P^0_{\bar{c}s}$ decay vertices have a projection of momentum that does not point back to the primary. However, many of the background events consist of K^* coming directly from the primary vertex.

5.4.5 DCA

The Distance of Closest Approach (DCA) is the minimum distance between two tracks. It helps to select two tracks that come from the same parent particle. The DCA criteria was applied to the K^* daughters K,π.

5.4.6 Pt2DK

Pt2DK is the sum of transverse momentum squared of the secondary vertex tracks, with respect to the direction of motion of the parent particle. It is proportional to the center of mass kinetic energy of the decay products (Q value). It helps to distinguish between charmed decay vertices with large Pt2DK and background events having typically smaller Pt2DK.

5.4.7 Pt balance

Pt balance is defined as the vector sum of all secondary tracks momentum components, transverse to the parent line of flight (primary - secondary). Pt balance should be zero. However, if some of the decay products remain undetected (neutral particle, detector inefficiency) the Pt will not be balanced.
The difference between Pt balance and Pt2DK is that while Pt balance is a vector sum indicating errors in identifing all the correct vertex tracks, Pt2DK is a sum of

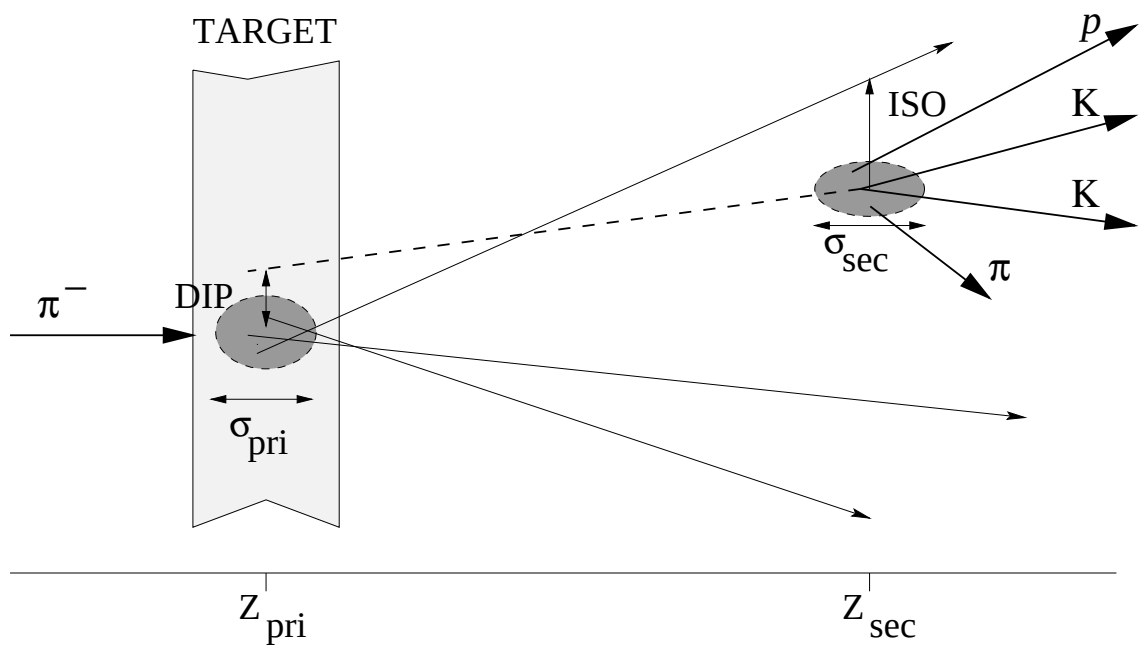

Figure 5.1: Illustration of some of the variables. A π^- particle (left side) hits one of the target foils (gray). The pentaquark production vertex (primary) is located within the target foil (dark), while the decay vertex (secondary) is located outside of the target foil (dark ellipsoid on the right). The four pentaquark daughter tracks (K,K,π,p) originating from the secondary vertex, can be seen on the right side. The notations "pri" and "sec" stands for the primary and secondary vertices, respectively.

5.4.1 SDZ

The SDZ variable is defined by

$$SDZ = \frac{Z_{sec} - Z_{pri}}{\sqrt{\sigma_{pri}^2 + \sigma_{sec}^2}} \tag{5.2}$$

where $Z_{pri,sec}$ are the Z coordinates of the primary and secondary vertices and $\sigma_{pri,sec}$ are the errors in the Z position of the two vertices, respectively.
The SDZ is an efficient momentum independent tool that cleans background events from charmed events. The SDZ parameter is lifetime dependent - for long lived particles higher SDZ values can be used without significant loss in efficiency.

5.4.2 ISO

The name ISO is derived from isolation. The ISO variable is the distance on the X-Y plane between the secondary vertex and any track that doesn't belong to it (see fig. 5.1).

and assume it is a signal; one then may be tempted to adopt a biased set of selection criteria, resulting in a false signal (see section 5.5).

5.3 The analyzer

The analyzer was a program that read the DST data tapes, and by using a pre-defined set of selection criteria (see section 5.4), recorded the selected interesting events into a data base (we used the CERN/PAW package) for further analysis.

The $D_s \rightarrow K^*K \rightarrow KK\pi$ analyzer passed over the tracks of each event, and searched for two tracks with opposite charges having a Čerenkov kaon probability higher than the a-priori value (see section 3.1.5). It then searched for an additional track that, assuming it to be a pion, can form with one of the kaons a neutral K^* candidate (mass window of $\pm$ 50 MeV/c^2). Some selection criteria (see section 5.4) were checked and the D_s mass was calculated. Candidates that qualified the micro strip set of selection criteria (see table 5.1), with mass in the region 1.79-2.05 GeV/c^2 were recorded in the data base.

The $P^0_{\bar{c}s} \rightarrow K^*Kp \rightarrow KK\pi p$ analyzer was based on the D_s analyzer (except for the calculation of the D_s mass) with an additional loop over the tracks, in order to search for a track having a Čerenkov proton probability higher or equal to the a-priori value (see section 3.1.5). The total charge of the four tracks was required to be neutral to form a $P^0_{\bar{c}s}$ candidate. Some selection criteria (see section 5.4) were checked and the $P^0_{\bar{c}s}$ mass was calculated. Candidates that qualified the micro strip set of selection criteria (see table 5.1), with mass in the region 2.4-3.1 GeV/c^2 were recorded in the data base.

5.4 Analysis parameters

In this section, all the selection criteria used in the different stages of the data processing are introduced. In figure 5.1 some of the variables are illustrated.

due to low efficiency and high background level. The Ξ_c has a larger production cross section than that of the pentaquark, and the unsuccessful search for the Ξ_c led us to discontinue our effort to search for the pentaquark in this decay mode.
The detection of the $\Psi_{D_s^- n}$ term is also not practical for the E791 experiment, leaving the $\Psi_{D_s^- p}$ term as the decay chosen for this research.

In a spectator decay model the off mass shell D_s meson is expected to approximately retain the same decay channels and branching ratios as an on mass shell D_s meson, except of phase space effects (see section 7.1). Some of the D_s major decay channels, that contain only charged particles in the final state, are listed in table 2.2. It can be seen that both $\phi\pi$ and K^*K channels have a relatively large branching ratio. The $\phi\pi$ ($P^0_{\bar{c}s} \rightarrow \phi\pi p$) channel was already searched for, by a fellow student from the E791 collaboration. Therefore, the K^*K ($P^0_{\bar{c}s} \rightarrow K^*Kp$) channel was selected for this work. It is important to state that although the analyses may look similar, the large differences between the ϕ and the K^* particles required a very different analysis for each channel. A comparison of the two decay modes is done in chapter 7.

5.2 Method of analysis

The expected low cross section of the pentaquark presents a challenging problem. The open trigger used in the E791 experimental setup had minor selectivity, forcing the analysis to be highly selective. The best way to detect rare particles is to achieve high sensitivity, defined by

$$Sensitivity = \frac{Signal}{\sqrt{Background}}. \tag{5.1}$$

High sensitivity fights the background level and makes it possible to detect the signal over the background fluctuations. Efficiency is an important parameter that should be maintained at a reasonable level, since low efficiency may cause the signal to vanish.

The analysis was done in a "blind" method: to avoid bias, one does not look at potential candidates for signal before deciding upon the final set of selection criteria. Such bias may arise when one is searching for a decay which is not expected to be observed, and observes a candidate; one then assumes it is background and is tempted to tighten the selection criteria in order to eliminate it. The problem with this procedure is that one may eliminate a real signal event, resulting in an incorrect upper limit for the decay. Alternatively, one may detect a background fluctuation

Chapter 5

The analysis

5.1 Selection of the decay channel

The pentaquark doublet wave function (see equation 2.19) contains information about possible decay modes. The color octet term (Ψ_{5q}) is not recommended for a search since its normalization is difficult. Moreover, the branching ratios of the color octet term into different final states are difficult to estimate.
The terms which are composed of the Σ particle ($\Psi_{D^-\Sigma^+}$, $\Psi_{\bar{D}^0\Sigma^-}$) have a very low detection efficiency as in 99.9% of the cases the Σ particle decay products consist of at least one neutral particle (the E791 spectrometer has low efficiency and momentum resolution for detecting neutral particles).
The terms which are composed of the Λ particle ($\Psi_{\bar{D}^0\Lambda}$, $\Psi_{D^-\Lambda}$) are problematic. It is expected that once the pentaquark decays through a Λ-D channel, the off-mass-shell D meson will decay via the same decay modes as the corresponding on-mass-shell meson. The Λ remains spectator in the decay process since it is more stable. In this decay there will be two secondary vertices. In the first the pentaquark decays into a $\Lambda K\pi$, $\Lambda K2\pi$, $\Lambda K3\pi$, or any other combination of a Λ particle and the decay products of a D meson. The second vertex is where the Λ decays, located downstream of the first one. A vertex can be reconstructed well only if it is located upstream of the first magnet (placed 1.8m downstream of the last target). Due to the relatively long lifetime of the Λ particle ($\tau_\Lambda = 2.6 \cdot 10^{-10}$sec), the reconstruction efficiency of the Λ vertex is smaller than other two-prong vertices. Moreover, the Λ usually decays downstream of the SMD, where the poor resolution of the DC stations (see section 3.1.3) results in a high background level (usually, a Λ vertex located in the DC region can be correlated with more then one SMD secondary vertex).
The decay $\Xi_c \to \Lambda K^+\pi^-$ is practically identical to the expected pentaquark decay channel $P^0_{\bar{c}s} \to \Lambda K^-\pi^+$. A search for the Ξ_c revealed no signal in that decay mode,

The generic MC helped understanding the various sources of background, and finding ways to reduce it. It pointed out different possible sources of background, such as $D^0 \to K\pi\pi\pi$, $D_s \to KK\pi$, $D^{\pm} \to KK\pi$, $\phi \to KK$. These decay products (with or without additional particles that could originate from the primary vertex) were misidentified as K, K, π, p and formed a background in the pentaquark mass spectrum. The Čerenkov counters were not perfect and such misidentification could happen.

The misidentification sources were examined in the data and those that were found, were eliminated from the final sample as described in section 5.7.

The logic behind the data reduction process was to collectively reduce as much data as possible by choosing more stringent selection criteria at each stage. Each level of the stripping process had all the selection criteria as the previous ones (or tighter), and usually some additional requirements.

4.2 The pentaquark Monte Carlo

A massive use of Monte Carlo (MC) computer simulations helped to study the pentaquark signature characteristics and to optimize the selection criteria. The Lund package of CERN was used in our experiment. Special treatment was still needed in order to produce the pentaquark, which was not included in Lund table of particles.

In order to simulate the $P^0(\bar{c}, s, u, u, d)$, the charm-strange Ξ_c^0(c,s,d) particle was chosen as a starting point. Its mass was changed to 2.83 GeV/c^2 (in the middle of the expected mass range), and the decay modes were changed to $P^0_{\bar{c}s} \rightarrow K^*Kp \rightarrow K^+K^-\pi p$ in order to simulate the selected decay mode (see section 5.1). A sample of 260K events was generated at a mass of 2.83 GeV/c^2, and a 220K sample at a mass of 2.75 GeV/c^2 in order to study the mass dependence of the efficiency.

In order to study discrepancies between MC and data, two MC samples of well known particles were made. The MC and data signals of $D^0 \rightarrow K\pi\pi\pi$ (taken from a dedicated sample of this decay) were compared in order to study discrepancies in the vertex parameters. The $D_s \rightarrow K^*K \rightarrow K^+K^-\pi$ MC and data signals were used to check Čerenkov distributions. The D_s MC sample was used for evaluation of the efficiency for D_s detection as well (see section 6.5). The D^0 and D_s samples had 400K events each. The results of the study appear in chapter 5 and in section 6.4.

4.3 The generic Monte Carlo

The sample of generic MC consisted of one million charm decays, made to simulate signals of all charm particles according to their known production cross sections and branching fractions. This sample simulated the behaviour of background, with one major advantage over the data background: MC events had truth table attached from which one could verify the origin of each track and vertex.

only a subset of E791 data sample.

The more stages the data reduction process passed, the more enriched the data sample became. Thus, at the sub-stripping stage, only few analyses could share the same code. The pentaquark sub-strip routine was based on Stream A tapes, and selected two pentaquark decay channels: $P^0_{\bar{c}s} \rightarrow \phi\pi p \rightarrow KK\pi p$, and $P^0_{\bar{c}s} \rightarrow K^*Kp \rightarrow KK\pi p$. The selection criteria (see section 5.4) used in the sub-strip routine were also common to other particles, such as the D_s and the D^0 mesons. The large signals of the D mesons were already obtained at that stage and were used to adjust a very mild set of selection criteria. Table 5.1 lists the sub strip selection criteria. The output of the sub-strip consisted of about one hundred tapes. It took about a month to pass the sub-strip output tapes through a micro-strip, creating 1-2 tapes of the final sample (see fig. 4.1).

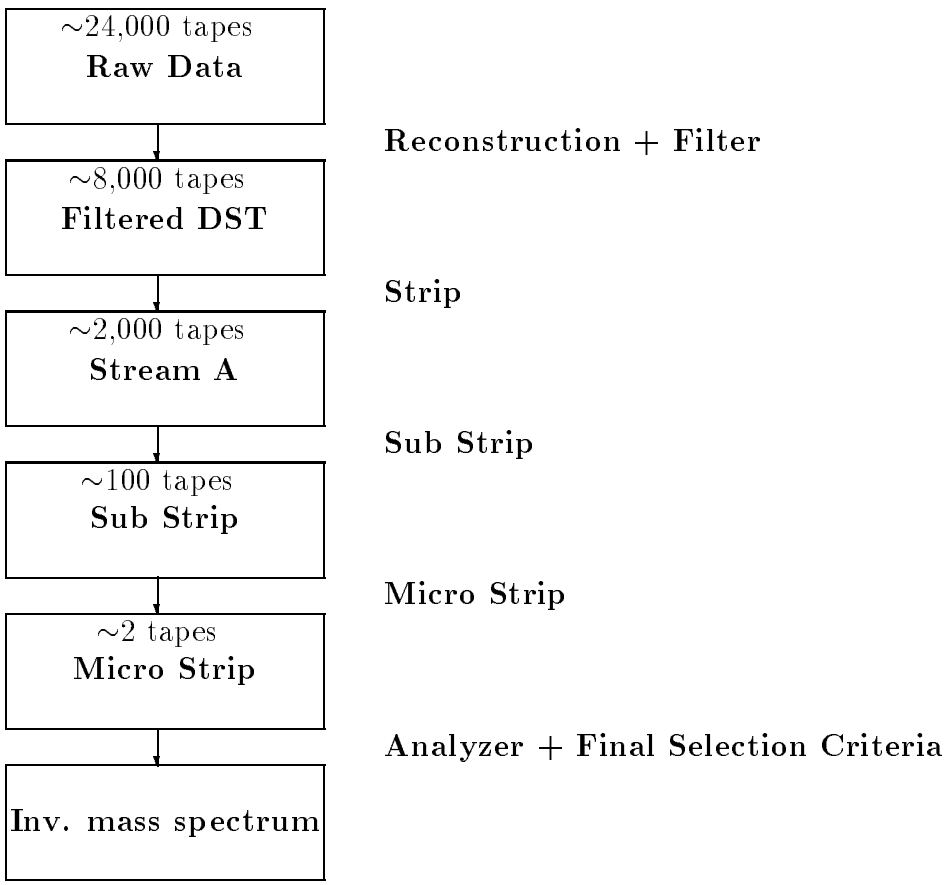

Figure 4.1: Data reduction diagram

(and Λ) particles in the SMD and in the first DC station. The K_s^0 decay vertex had to be separated by at least 15 standard deviations from the primary vertex (SDZ > 15; see section 5.4.1) - i.e. the distance between the z position of the primary and secondary vertices had to be at least 15 times larger then the error of that quantity.

- A Λ particle.
  The Λ is a long-lived particle, that appears in many of the charm decays. The filter routine detected Λ particles by their proton - pion decay vertex, which had an invariant mass close to the Λ mass. The Λ decay vertex was usually located in the first DC station, where the vertexer routine (see section 4.1) did not look for vertices. Therefore, a special designed routine searched for Λ (and K_s^0) particles in the SMD and in the first DC station. The Λ decay vertex had to be separated by at least 20 standard deviations from the primary vertex (SDZ > 20; see section 5.4.1) - i.e. the distance between the z position of the primary and secondary vertices had to be at least 20 times larger then the error of that quantity.

- A ϕ particle.
  The ϕ particle is a resonance, that appears in the pentaquark decay $P^0_{\bar{c}s} \rightarrow \phi\pi\mathrm{p}$. The filter routine detected ϕ particles by their two kaons' decay, which had an invariant mass close to the ϕ mass. During reconstruction of the last third of E791 data sample, the ϕ filter routine was replaced by a pentaquark filter routine. It helped to reduce the number of output tapes at the filter stage.

Events that passed these selection criteria were fully reconstructed, packed with the raw data, and passed to the Data Summary Tapes (DST).

Reconstruction and filtering were general processes for the whole E791 analysis, while the strip and its following processes were built out of few specific routines added together. In order to reduce the amount of data, the strip output was divided into two streams, labeled "Stream A" and "Stream B". Each analysis had its own specific stripping routine. Stream A had stripping routines for detection of charm decay vertices, based on the vertex list; while stream B had stripping routines for detection of long-lived particles: K_s^0, Λ, Ξ, Ω, a routine that detected the ϕ particle, and a special routine that detected diffractive jets. The stripping process was not a heavy CPU time consumer since its input tapes already contained physical information, and were

ciency). About 8% of the tracks were reconstructed from noise in the SMD detectors, and did not correspond to real tracks.

The vertexing algorithm took into consideration only PWC and SMD tracks. Primary vertices were formed by intersecting beam tracks with at least two downstream tracks. Other tracks were added to the primary vertex as long as the χ^2/dof calculated from track's impact parameters was not inflated beyond ten. The intersection was constrained to be in or near a target foil. Primary vertex reconstruction efficiency was 95% (meaning that in 95% of MC events, the primary vertex location was found). Secondary vertices were reconstructed from tracks taken from the track list, with momentum greater than 2.0 GeV. Primary vertex tracks could be included in a secondary vertex, however a track could only be used in one secondary vertex. Vertices were ordered in a vertex list by their χ^2. Secondary vertices were found first by combining two tracks with the smallest distance of closest approach which intersect downstream of the primary vertex. Other tracks were added until the χ^2/dof of the vertex inflated beyond ten. Secondary vertex reconstruction efficiency for charm decay was $\approx$17% (meaning that in $\approx$17% of MC charm decay vertices the vertexing algorithm found the secondary vertex, but not necessarily with the same tracks).
Most of the losses were short-lived decays removed by the vertex-separation demand in the filter. Roughly 9% of reconstructed secondary vertices did not correspond to real vertices.

Events that had a primary vertex, and at least one of the following features, were selected by the filter:

- A secondary vertex.
  At least one secondary vertex, well separated from the primary vertex, appeared in the vertex list. A two-prong secondary vertex had to have SDZ >6 (SDZ definition appears in section 5.4.1), while vertices with larger number of prongs had to have SDZ >4.

- A K_s^0 particle.
  The K_s^0 is a long-lived particle, that appears in many of the charm decays. The filter routine detected K_s^0 particles by their two pions' decay vertex, which had an invariant mass close to the K_s^0 mass. The K_s^0 decay vertex was usually located in the first DC station, where the vertexer routine (see section 4.1) did not look for vertices. Therefore, a specially designed routine searched for K_s^0

Chapter 4

The data sample

4.1 Data processing

The data acquisition system recorded 24,000 tapes of raw data, which are equivalent to 50 Terabytes. The raw data information was digitized detector information, that was not directly usable for physical analysis.
The reconstruction program converted the raw data into tracks and vertices, with physical information such as position, slope, momentum, charge, Čerenkov probabilities, and error matrices. The same reconstruction program was executed on four computer farms, with up to 20 nodes working in parallel in each farm; nevertheless it took more than three years (equivalent to 10,000 MIPS years) to accomplish reconstruction of the raw data sample.

The reconstruction program had three stages. Beam tracks, tracks in the SMDs, PWCs and DCs, momentum and vertices were reconstructed in the first stage. Based on this information, the filter in the second stage weeded out events that did not pass a mild set of selection criteria. Those events that passed the filter stage, were fully reconstructed by adding Čerenkov and calorimeter information found in the third stage.

The tracking stage converted hits from the SMDs, PWCs, and DCs into position, trajectory, slopes, and errors. Tracks were ordered in a track list by their Chi Square per Degree of Freedom (χ^2/dof), where χ^2/dof was calculated from the difference between the projected positions of tracks and the actual hit used. Tracking had to be performed before vertexing could begin. Monte Carlo studies showed that tracking reconstruction efficiency was 67%. The efficiency is defined as the number of reconstructed MC tracks over the number of all MC charged tracks, regardless of their direction (the detector acceptance is responsible for the major part of the ineffi-

- **Event Buffer Interface**
  Event Buffer Interface (EBI) controlled communication between buffers and CPUs. One CPU was allowed to control the buffers at a time. Once a CPU finished reading data, the EBI enabled control to the next available CPU.

- **Tape Drives**
  A total of 42 Exabyte 8mm tape drives accepted packed events from VME crates through SCSI interfaces. Each VME crate was connected to 7 tape drives with two SCSI busses. Each tape drive wrote 0.24 MB per second, single density to 8mm video tapes that can hold 2.2 GB.

- **Control Computer**
  A VAX computer ran the user interface program. It was capable of down-loading all commands to VMEs, pulling out events for online checks of all spectrometer components status. The user could also control loading and unloading of tapes and start and end runs.

topics could share the same experiment with large flexibility in applying individual selection criteria for the different analyses. It also reduced trigger bias in charm event selection. More detailed information about the trigger can be found elsewhere [25].

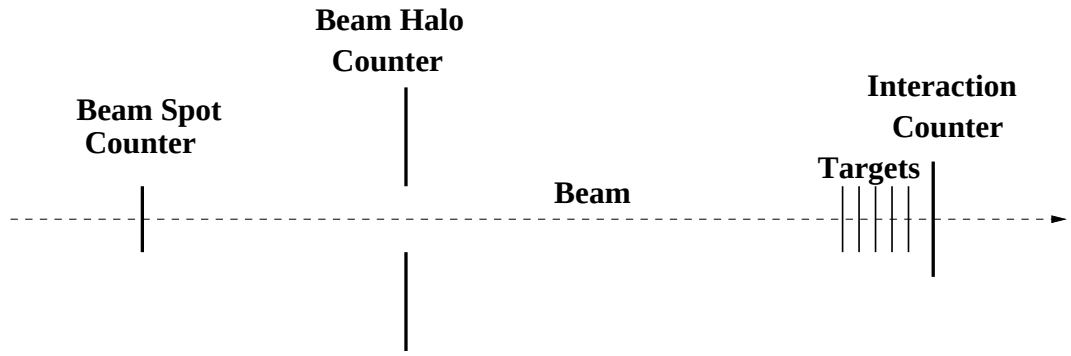

Figure 3.3: The Pretrigger

3.3 Data acquisition

A high speed Data Acquisition (DA) system, capable of handling 20,000 events and logging 9.6 MB per second was designed. The DA system read out 24,000 channels in 50 μsec during spill time. Events were accepted, compressed, and written continuously (during spill and interspill) to 42 Exabyte tape drives. More than 24,000 data tapes were recorded in the 6 months running period during 1991/92, corresponding to $2{\cdot}10^{10}$ events.

The data acquisition system, described in details elsewhere [31], was composed of five main parts:

- **Buffers**
  A total of 8 First In First Out (FIFO) buffers with a total of 640MB were used to store all digitized data from the detector. They could store roughly 100,000 events.

- **VME crates and CPUs**
  Event records were assembled by 6 VME crates that read data from the buffers. Each VME crate had 9 Motorola micro processor units, which compressed and formatted the data. Once an event record was assembled, it was sent to output tape drives.

The importance of the muon detection system was to further improve the particle identification of muons needed for semi-leptonic decays, the search for flavor changing neutral currents, etc. More detailed information about the muon system can be found elsewhere [25].

3.2 The trigger

A two level trigger that used no tracking or vertexing information enhanced the sample with charmed events. The first level was a fast (160 ns) pretrigger that detected the beam particle and the occurrence of an interaction. The pretrigger allowed early digitization to begin, after it checked that (see fig. 3.3):

- The beam spot counter registered exactly one beam pion.
  In order to avoid multiple beam particles, that could confuse later analysis, an event was rejected if the beam spot counter detected more than one beam pion.

- The beam halo counter had no signal.
  Veto events where beam pions strayed too far from the beam axis. Such events were rejected since they had a poor spectrometer acceptance and tracking, and they could even miss the targets.

- The interaction counter registered at least four minimum ionizing particles.
  While the previous counters inspected the beam particle, this criterion checked the existence of an interaction with the target. In order to verify that some interaction took place, the interaction counter pulse height should be higher than four times of its minimum pulse - which happened when no interaction took place and only one beam pion passed through the detector.

The second level trigger was a loose E_t requirement which enabled recording interactions with E_t of 4 GeV or more. Charmed events are characterized by large transverse momentum. All the calorimeter phototube signals were summed, using a weight function that gave more weight to signals further from the beam axis. A signal was sent to the trigger indicating whether the sum qualified the E_t trigger demand.

The philosophy behind this open trigger was to record as many events as possible and to apply tighter selection criteria during offline data analysis, when time and computing resources were more available. Consequently, many different research

3.1.6 Calorimeters

All the detectors described so far provided a way to measure some properties of a particle passing through, with as little disturbance as possible. The calorimeters, on the other hand, are built in such a way that a particle will deposit most of its kinetic energy in them. The basic calorimeter's concept is to use multiple detector layers and measure the amount of energy the particle deposits in each layer. The total kinetic energy of the particle is determined by adding the output of all the layers.

Two calorimeters were used in the spectrometer: the Segmented Liquid Ionized Calorimeter (SLIC) and the Hadrometer. They were used to identify electrons and photons through observation of electromagnetic showers, and to identify neutral hadron candidates. The SLIC was an electromagnetic calorimeter, composed of 60 layers of oil-based scintillator (NE235H), aluminum and teflon, which provided good e/π separation. Particles interacting primarily through electromagnetic interactions were identified by the SLIC. Photon and electron interactions were identified by narrow shower shapes and the amount of energy they deposited in the detector, while hadronic interactions were discriminated by their wide shower shapes.
The Hadrometer was located just downstream of the SLIC and had 36 layers of 2.5 cm thick steel, interleaved with 1 cm thick plastic scintillators. The difference between the energy deposited in the front and rear parts of the Hadrometer provided information used to separate muons from hadrons.

The calorimeters' information was used as a feedback to the Čerenkov - if a muon signature was detected by the calorimeter, the Čerenkov probability for a muon was increased. Another important use of the Hadrometer was to provide the real time E_t trigger (see section 3.2). More detailed information about the SLIC and Hadrometer can be found in [29] and [30], respectively.

3.1.7 Muon detection

The muon detection system was placed downstream of the Hadrometer. It consisted of 1m thick steel wall that stopped hadrons, followed by two arrays of scintillator planes. The main principle was to take advantage of the muon low interaction cross section with media. Presumably only muons could pass through the whole detector, including the two calorimeters and the thick iron wall, and hit the muon detection system.

taken from the previous experiment (E769). Their exact number is not important since they were only used as benchmark values (they really depend on center of mass energy, momentum, etc.).

When ambiguity occurred between the three particles, they all had Čerenkov probabilities relative to their a-priori probabilities normalized so that their sum was 1. Partial ambiguity between some of the particles was treated in the same manner; For example, a K-p ambiguity led to 0.75 kaon probability and 0.25 proton probability (the selection criteria used in the analysis had to take into considerations the ambiguity regions and had to combine Čerenkov criteria with momentum criteria in order to achieve better results - see section 5.4 and table 5.1).

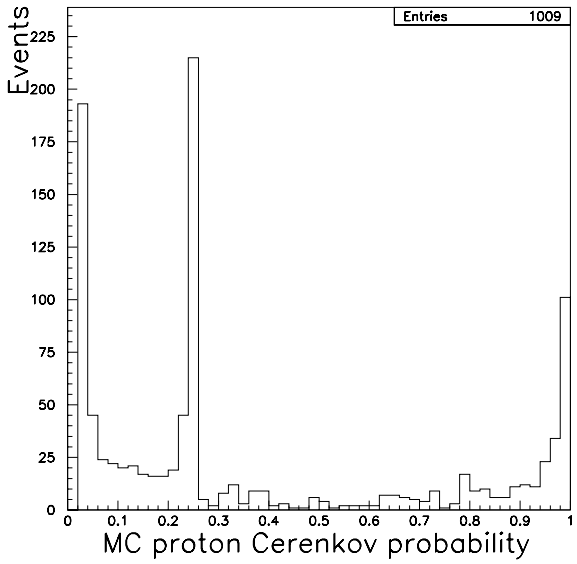

Figure 3.2: The Čerenkov probability of MC protons. The distribution shows the a-priori peak at 0.04, the proton-Kaon ambiguity peak at 0.25, and a positive proton identification peak at 1.00.

Figure 3.2 shows the Čerenkov probability of MC protons. Three peaks can be seen at the values of 0.04, 0.25 and 1.00. The peak at 0.04 originates from the ambiguity between π,K and p. The peak at 0.25 originates from the ambiguity between K and p, while the third peak reflects those cases where the Čerenkov positively indentified a proton.
More detailed technical information about the Čerenkov counters can be found elsewhere [28].

Table 3.1: Threshold momenta in the Čerenkov counters

Counter	Particle Type				
	e	μ	π	K	P
Č1 [GeV/c]	~ 0.03	~ 4	~ 6	~ 21	~ 40
Č2 [GeV/c]	~ 0.04	~ 8	~ 11	~ 39	~ 74

The different threshold momenta of the particles resulted in different signatures for each momentum region. Table 3.2 shows the response of the two Čerenkov counters to the charged hadrons in different momentum bins, the + (−) sign denotes those cases where Čerenkov radiation is (is not) emitted. Muons and pions have similar mass, hence the Čerenkov lacks the ability to distinguish between them and another detector is to be used (see section 3.1.7). The threshold momentum of electrons was very low, thus always emitting Čerenkov radiation in both counters.

Table 3.2: Čerenkov counters light response

Momentum	π		K		p	
(GeV/c)	Č1	Č2	Č1	Č2	Č1	Č2
<6	−	−	−	−	−	−
6 - 11	+	−	−	−	−	−
11 - 21	+	+	−	−	−	−
21 - 40	+	+	+	−	−	−
40 - 75	+	+	+	+	+	−
>75	+	+	+	+	+	+

It is important to notice that in the momentum range 21 to 40 GeV/c (see table 3.2) π,K and p can be identified unambiguously. However, in all other momentum ranges there is an ambiguity between some or all of the particles. In the range 0-6 GeV/c none of the particles radiate, leaving the π,K,p ambiguous. In the range 6-21 GeV/c only pions radiate, leaving the kaons and protons ambiguous. Ambiguity had three forms: π,K,p (0-6 GeV/c, and above 75 GeV/c); K,p (6-21 GeV/c); and π,K (40-75 GeV/c).

The Čerenkov particle identification algorithm compared the amount of light collected for each particle trajectory and that expected for an e, μ, π, K and p having the track's momentum. The algorithm calculated the probability that the particle was of a given type, by using compound Poisson distributions. The probability was multiplied by the a-priori likelihoods that e, μ, π, K and p were produced in the collision: 0.02, 0.01, 0.81, 0.12, and 0.04 respectively. These a-priori likelihoods were

- To connect tracks found by the SMDs to tracks found by the DCs.
  Two additional stations of PWCs were placed just downstream of the SMDs, with the first DC station, D1, placed in between them. The PWCs tracks information increased the efficiency of the offline procedure that connected a SMD track to a DC track.

The PWCs were filled with a gas mixture of 82.7% Ar, 17% CO_2 and 0.3% Freon. The operation principle of PWCs was similar to that of the DCs, except that the wires were denser, resulting in a shorter drift time. The PWC weak signal was amplified by a Proportional Charge Operational System (PCOS). The position in space was obtained from the intensity difference of signals from two adjacent wires (the drift time was not measured). The advantage of PWC over the DC was their speed (4μs) and resolution (300μ), while their disadvantage was the weak signal that required an amplification. More detailed information about the PWCs can be found elsewhere [25].

3.1.5 Threshold Čerenkov counters

High quality particle identification was needed to reduce the background associated with incorrect identification of tracks. The detector had two multi-cell threshold Čerenkov counters Č1 and Č2, in order to discriminate between protons, kaons and pions.

A charged particle radiates Čerenkov radiation if its velocity is higher than the light velocity in the medium. For index of refraction n, the speed of light in the medium is c/n, where $n > 1$ and c is the speed of light in vacuum. A charged particle with velocity of $v > c/n$ will radiate a cone of light around its path. The cone is defined by $sin(\theta) = c/vn$ where θ is the cone opening angle. The intensity of the Čerenkov radiation increases as the momentum increases.

The two Čerenkov counters Č1 and Č2, were filled with different gas mixtures (Č1 had 100% N; Č2 had 80% He and 20% N). This resulted in two different indices of refraction, and two different threshold velocities (see table 3.1). The Čerenkov radiation was collected by a plane of spherical mirrors, that reflected the light into photomultiplier tubes. During offline analysis the momentum for each track was calculated.

3.1.2 Magnets

The task of the magnets was to determine the momentum and electrical charge of charged particles. This was basically done by measuring the entrance and exit trajectories of each particle in the magnet. The magnetic part of the spectrometer consisted of two horizontally bending dipoles with a P_t kick of 0.21 GeV/c in the first magnet and 0.32 GeV/c in the second. The two kicks enabled a momentum measurement with high resolution given by the expression [26]:

$$\frac{\delta p}{p} = \frac{3.33(\delta x)p}{r \int Bdl}, \tag{3.1}$$

where δx is the resolution in x and r is the lever arm to the Drift Chambers.

3.1.3 Drift chambers

Downstream tracking and momentum analysis were accomplished by fitting information provided by four stations of Drift Chambers (DC) D1-D4, with a resolution of 300-450μm. A total of 35 DC planes were used to track particles passing through the magnets and the Čerenkov counters, and connect them to tracks found by the SMD.

The DCs were filled with a gas mixture of 89% Ar, 10% CO_2 and 1% CF_4. Each DC plane alternated between wires maintained at 0 Volts and -2 KVolts. Whenever a charged particle passed through the gas mixture, it left a trail of ionized gas and electrons. The resulting free electrons, accelerated by the electric field, traveled towards the wires in the chamber, producing a secondary ionization which resulted in an amplified signal. The position in space was obtained from measuring the drift time The drift time was measured between the DC wire pulse and the interaction counter pulse, and was later normalized according to the z position of each DC place and the electronics delay time. Tracks were categorized by the number of DC stations which recorded their path. More detailed information about the drift chambers can be found elsewhere [27].

3.1.4 Proportional wire chambers

Proportional Wire Chambers (PWCs) were used for two tasks:

- To measure the beam direction in high precision.
  Two stations of PWCs were placed 12 and 31 meters upstream of the targets, giving resolution of 300μm. The fine resolution, combined with the large distance provided excellent beam information (angular resolution of 10 μrad).

3.1 The E791 spectrometer

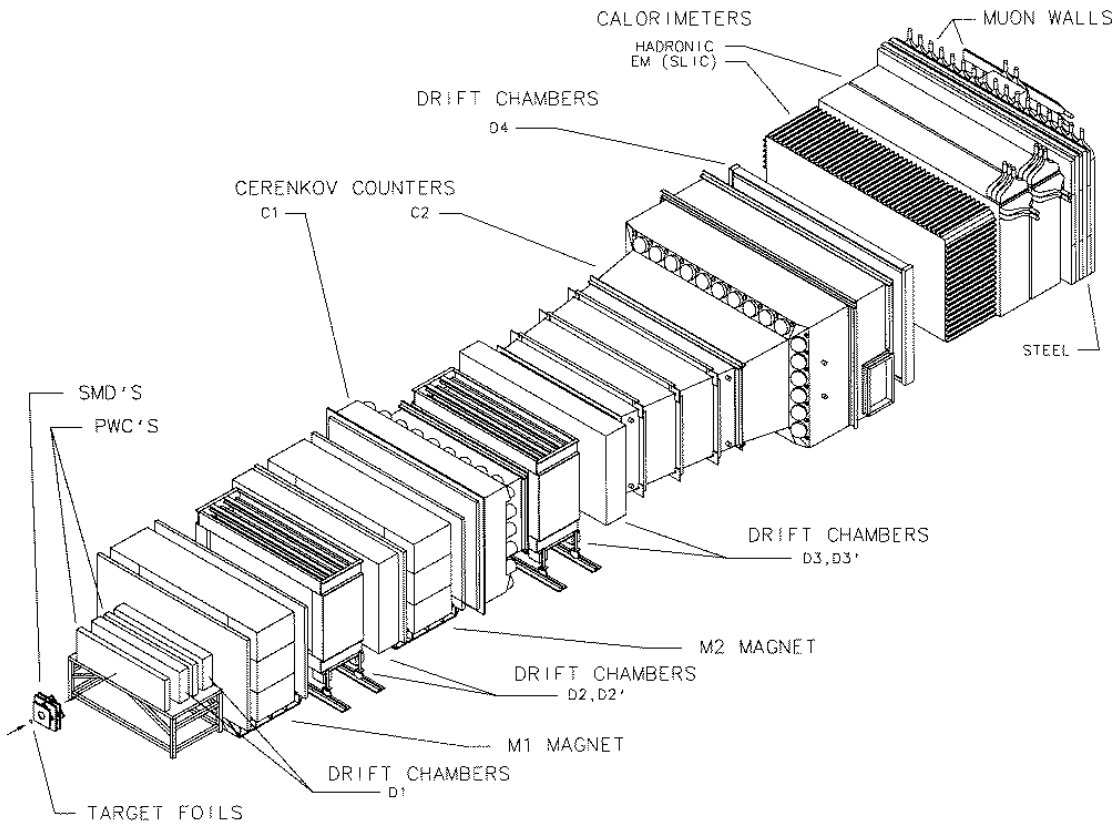

Figure 3.1: The E791 Spectrometer.

3.1.1 Silicon microstrip detectors

The front end of the spectrometer consisted of 23 planes of silicon microstrip detectors (SMD) that covered 100 mrad solid angle. Each SMD plane was a 300 μm thick p-n junction diode operated at reverse bias. Six of the SMD planes were placed upstream from the targets in order to detect the beam direction, while the other 17 planes were placed downstream of the targets for reconstructing tracks and vertices. A charged particle that passed through an SMD plane ionized the n-type silicon that produced on average 25,000 electron-hole pairs - a sufficient amount of charge for creating a measurable pulse. The SMD resolution ranged from 7.2 μm near the center to 60 μm near the edge. Each SMD plane had a detection efficiency of 90-99%. The total averaged resolution for the charm decay vertex was 350 μm in Z direction (parallel to the beam) and 6 μm in the X and Y directions. More detailed information about the SMD and its readout system can be found elsewhere [24],[25].

an order of magnitude larger than any previous experiment [23]. The experiment succeeded to surpass its goal by a factor of two, and had more charm decay statistics than any other experiment at this time.

A negative pion beam of 500 GeV/c interacted with target nucleons. The beam cycle was 57 seconds, and was split into two parts, the spill and interspill. During the 22 second spill, pions were sent to the E791 target, and during the interspill the accelerator ramped up for the next spill. The target consisted of a series of foils: first a 0.5 mm thick platinum foil followed by four 1.5 mm thick carbon foils (milled from industrial diamond drill bits). Spacings between the foils were set to 15 mm to ensure enough decay space outside the target foils for charm. The targets arrangement was optimized for the detection of short lived states decaying in the air gaps between foils and reduction of multiple-scattering while providing an interaction rate of about 40 KHz. The use of targets from different materials can be used for research of atomic mass dependence of diffractive jets, charm cross section, and more.

In this chapter the characteristics of the E791 spectrometer, the trigger and the data acquisition system are described.

Chapter 3

The experiment

The discussion in chapter 2 determined the main parameters of this search. We are searching for the pentaquark $P^0_{\bar{c}s}$ in the 2.75-2.91 GeV/c^2 mass region, having a production cross section a few percent of that of the D_s particle, and a lifetime of the order of 10^{-12}-10^{-13} sec.

An experiment in which the pentaquark can be searched for, should satisfy the following requirements:

- A reaction in which charmed-strange particles, such as D_s^- ($\bar{c}$,s), are produced.
- High statistics - the pentaquark production cross section is expected to be two orders of magnitude lower than for the D_s.
- High quality particle identification for reducing the background associated with incorrect identification of tracks.
- An experimental setup that allows observation of the pentaquark decay vertex, with a low background level and a good invariant mass resolution.

Experiment E791, performed at Fermi National Accelerator Laboratory (FNAL) - a high statistics charm physics experiment - was found appropriate for the pentaquark search.

Originally, the spectrometer (see fig. 3.1) was designed for E516, a photoproduction charm experiment carried out in the early 1980s. Since then, the spectrometer has been upgraded to further investigate charmed particles. E691, a photoproduction experiment was the first upgrade, followed by upgrades for hadroproduction experiments E769 and E791. During a six-months period ending in January 1992, E791 recorded over 2 $\cdot 10^{10}$(!) π^--nucleus interactions (50 times more than E769), producing 50 Terabytes of data. The goal was to reconstruct 100,000 charmed particles,

particles (see table 2.3).

annihilation of the $\bar{c}$ quark or a W exchange via the Cabibbo suppressed and allowed transitions; these kind of signatures are very hard to detect in an experiment.

A search for a bound pentaquark may be done in any of these decay modes. The D_s-p component has a mass 70-150 MeV lower than all other "color-singlet" components, implying that this may be the dominant component in a weakly bound deuteron-like pentaquark. The detection efficiency of the spectrometer to the decay products should be taken into consideration as well (a spectrometer with a low detection efficiency for neutral particles may not be used for a Σ based decay channel since one of the Σ daughters is probably (99.9%) a neutral particle).

A search for an unbound pentaquark can be done via the D_s-p decay, which has the lowest mass among the "color-singlet" components. A highly unbound pentaquark might decay also through other "color-singlet" components. Nevertheless, the D_s-p channel will always retain the largest phase space integral and presumably a larger decay width.

2.10 Expected lifetime of the pentaquark

The lifetime of the pentaquark depends on the structure of its wave function (see equation 2.19). The spectator model (see section 2.9) means that a decay through a "color singlet" channel results in one part (usually the charm meson) to decay off its mass shell. An off mass shell decay has a smaller phase space, which results in a longer lifetime. The "color singlet" charmed mesons components of the pentaquark wave function are the D_s, D^- and $\bar{D}^0$. Their lifetimes are listed in table 2.3.

Table 2.3: The lifetime of some charm particles.

Particle	Lifetime
$D_s^-(\bar{c}s)$	4.7×10^{-13} sec.
$D^-(\bar{c}d)$	10.6×10^{-13} sec.
$\bar{D}^0(\bar{c}u)$	4.2×10^{-13} sec.
$\Xi_c^+(csu)$	3.5×10^{-13} sec.
$\Xi_c^0(csd)$	1.0×10^{-13} sec.

Decay through the color octet component should reduce the pentaquark lifetime, but it is hard to estimate its effect. Consequently, lifetime of a bound pentaquark is expected to be in the range of 10^{-13}-10^{-12} sec. - of the same order as other charmed

$$\left.\begin{matrix}\bar{c}\\ s\end{matrix}\right\} D_s \qquad \left.\begin{matrix}\bar{c}\\ d\end{matrix}\right\} D^- \qquad \left.\begin{matrix}\bar{c}\\ u\end{matrix}\right\} \bar{D}^0$$

$$\left.\begin{matrix}u\\ u\\ d\end{matrix}\right\} p \qquad \left.\begin{matrix}u\\ u\\ s\end{matrix}\right\} \Sigma^+ \qquad \left.\begin{matrix}u\\ d\\ s\end{matrix}\right\} \Lambda \tag{2.20}$$

$$2.907\ GeV \qquad 3.058\ GeV \qquad 2.981\ GeV$$

In table 2.2 some decay modes of these particles are listed together with their branching ratios (BR) [22]. The relative strength of these components depends strongly on the binding energy. Once the pentaquark will decay via one of its "color singlet" wave function components, the three quarks in the baryon may act as spectators in the decay process, and remain in the final state as a nucleon, Λ or Σ. The remaining two quarks may create an off-mass-shell D_s, D^- or $\bar{D}^0$ meson that decays. Feynman diagrams describing the $P^0_{\bar{c}s} \to \phi\pi$p, and $P^0_{\bar{c}s} \to K^*Kp$ channels are shown in figure 2.5.

Table 2.2: Major decay modes of the "color-singlet" components of the pentaquark.

D_S^-		D^-		Σ^+		D^0		Λ	
Decay	BR	Decay	BR	Decay	BR	Decay	BR	Decay	BR
$\phi\pi^-$	3.6%	$K^+\pi^-\pi^-$	9.1%	$\rho\pi^0$	52%	$K^+\pi^-$	3.8%	$p\pi^-$	64%
K^*K^-	3.4%	$K^0\rho^-$	6.6%	$n\pi^+$	48%	$K^+\pi^-\pi^0$	13.9%		
$\phi\pi^+\pi^-\pi^-$	1.8%	$K^0\pi^-$	2.7%			$K^+\pi^+\pi^-\pi^-$	7.5%		
$K^+K^-\pi^-$	0.9%								

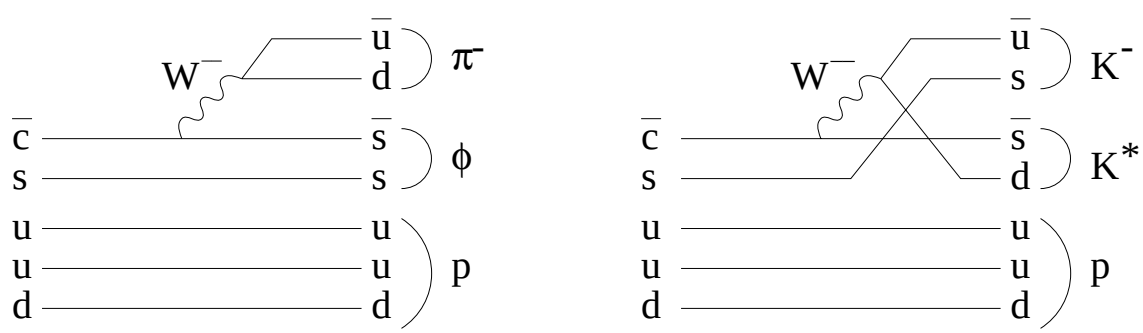

Figure 2.5: Feynman diagrams of the decays $P^0_{\bar{c}s} \to \phi\pi p$ and $P^0_{\bar{c}s} \to K^*Kp$.

The last part of the pentaquark wave function, Ψ_{5q}, suggests that other channels exist. Examples of these channels can be the decay of the pentaquark into $\Sigma - K$, $\Xi - K$, $N - \pi$, $N - K$, etc. The mechanisms of those decay modes is through direct

where B is $\sim$ 5-6 GeV^{-1}. Since the two-quarks and three-quarks states follow this formula, it is expected that the five-quarks state will obey this formula too. Integration over p_t yields [21]:

$$\sigma(P)/\sigma(D_s) \sim exp\{-B[M(P) - M(D_s)]\} \sim 10^{-2} \tag{2.18}$$

Each of the two production mechanisms described above can contribute to the total production cross section through the various components of the wave function. The predictions of the coalescence production and the full production are similar, which implies that the production rates are not sensitive to the details of the pentaquark inner structure.

2.9 Expected decay modes of the pentaquark

The pentaquark doublet ($\bar{c}sudd$, $\bar{c}suud$) wave function can be decomposed to three "color-singlet" and one color-octet components. The meaning of the "color-singlet" components is that the constituent quarks can be grouped to form meson-baryon (each with neutral color), while the color-octet component has no sub-set of quarks with neutral color. The pentaquark contains one anti-quark ($\bar{c}$) which can be coupled with an additional quark to form one of three possible mesons: $D_s^-(\bar{c}s)$, $\bar{D}^0(\bar{c}u)$, and $D^-(\bar{c}d)$. The overall wave function can be written as:

$$\begin{aligned} |\Psi_{P^0_{\bar{c}s}}\rangle &= \alpha_1|\Psi_{D_s^- p}\rangle + \alpha_2|\Psi_{D^-\Sigma^+}\rangle + \alpha_3|\Psi_{\bar{D}^0\Lambda}\rangle + \alpha_4|\Psi_{5q}\rangle \\ |\Psi_{P^-_{\bar{c}s}}\rangle &= \beta_1|\Psi_{D_s^- n}\rangle + \beta_2|\Psi_{D^-\Lambda}\rangle + \beta_3|\Psi_{\bar{D}^0\Sigma^-}\rangle + \beta_4|\Psi_{5q}\rangle \end{aligned} \tag{2.19}$$

where the first three terms in each equation represent the "color-singlet" components of the pentaquark and the last term represents the color-octet component. Each color singlet represents a few possible combinations and excitations (spin, angular momentum). Equation 2.19 is not a precise wave function, since the individual terms are not orthogonal; however, it is sufficient for our purposes. In general, whatever can be said about the pentaquark, holds true also for charge-conjugates particles.

The lightest "color singlet" combination is the $D_s^- N$ with a mass of 2.907 GeV, implying that a bound pentaquark must have a mass below that threshold (see 2.20).

at most. The probability for coalescing N particles is given by [18]:

$$N_c = \int f(x_i, p_i) C(x_i, p_i) \prod_{i=1}^{N} \frac{2\theta(p_i)\delta(p_i^2 - m_i^2) d^4 p_i}{(2\pi\hbar)^3} \cdot p_i^\mu d\sigma_\mu^i \tag{2.15}$$

where $f(x_i, p_i)$ is the distribution function of the coalescing particles in phase space, depending on 8N variables (x_i are the space-time and p_i are the momentum-energy coordinates of the N particles). $C(x_i, p_i)$ is the coalescence factor which measures the probability that the particles occupy the small phase space volume that allows the interaction. The last part of eq. 2.15 is the phase space and momentum conservation. The term $p_i^\mu d\sigma_\mu^i$ represents an integration over a spacelike hypersurface which counts the number of particles contained in the system by integrating the projection of the flux ($\sim p^\mu$) on the (timelike) surface normal vector ($d\sigma_\mu$).

The distribution function f of a pair is usually[1] taken as the product of two separate distribution functions f_1, f_2:

$$N_c = C \times f_1 \times f_2 \tag{2.16}$$

Evaluation of the coalescence integral (C) is different for each particle. Estimate of the pentaquark production cross section should take into account:

- The coupling of the meson-baryon states to the pentaquark spin-flavor state.
- Each meson-baryon channel accounts only for a part of the pentaquark wave function.

The result of the coalescence calculation for the pentaquark production cross section is of the order of 10^{-2}-10^{-3} of that of the D_s [19].

The second reaction mechanism is the full production of the pentaquark. This mechanism considers a production of all five quarks in the interaction. It is based on the empirically motivated equation which predicts reasonably well the production cross section of a mass M hadron for low p_t in central collisions [20]:

$$d\sigma/dp_t^2 \sim exp(-B\sqrt{M^2 + p_t^2}) \tag{2.17}$$

[1] In cases where the two coalescing particles are identical, quantum statistical effects can interfere. For example, the coalescence of Λ-Λ to form hypothetically a hexaquark is more complicated; however, in the pentaquark case there is no such problem.

More recent work on pentaquark based on the soliton model was carried out by C.K. Chow [7]. His results are similar to the above binding predictions and he predicts that the state $\bar{Q}ssud$ will also be stable against strong decay.

2.7 The instantons model

The instantons are a class of gauge fields with nontrivial topological properties. Instanton is the minimum of the Euclidean four-dimensional space-time action, i.e, it is the classical path for imaginary time. The name instantons comes from "instant" which expresses their structure in time. The instantons model has provided a qualitative understanding of a variety of nonperturbative features of QCD [16]. One of its important consequences is that the coupling of light quarks (u,d and s) to the instanton breaks its axial symmetry and causes the $\eta - \eta'$ mass splitting. Recent attempts to build a quantitative model of interacting instantons conclude that the QCD vacuum may be an instanton liquid, consisting of strongly interacting instantons [17].

One of the latest theoretical works on the pentaquark was carried out by Takeuchi, Nussinov and Kubodera [8]. The authors used the instanton-induced interactions on the hexaquark and the pentaquark and predicted that the hexaquark inner repulsion is stronger than that of the pentaquark. Considering the uncertainties in the intermediate attraction used by the authors, both exotic particles poses low binding potentials which are not sufficient to definitely predict the stability of any one of them.

2.8 Production mechanisms

The pentaquark production mechanism depends on its internal structure (sec. 2.9). There can be several ways in which the pentaquark may be produced; we will consider two reaction mechanisms: "coalescence production" and "full production".

In the coalescence production, N particles are being produced, and then fused into one particle [18]. For example, coalescence of p-D_s, Λ-$\bar{D}^0$, and Σ^+-D^- can form the $P^0_{\bar{c}s}$. For this to occur, the two systems must share a small volume of phase space: distances of the order of one Fermi and momentum difference of a few hundred MeV/c

Numerous improved versions of the MIT bag model have been developed, with a variety of purposes. One problem was to modify the model to include heavy quarks [12]. A use of the bag model to study flavored mesonic ($Q\bar{q}q\bar{q}$) and baryonic ($\bar{Q}qqqq$) states, where one heavy quark Q is associated with light quarks or antiquarks, was carried out by S. Zouzou, and J.M. Richard [13]. The bag radius R is larger for multiquark states than for ordinary hadrons; consequently, the strength of the chromomagnetic terms decreases.

2.6 The soliton model

Recently, the predictions of a stable pentaquark received further confirmation from calculations based on the soliton model (known also as Skyrme model).

In the limit of a large number of colors, QCD yields an effective Lagrangian that describes a nonlinear field theory of interacting mesons, and in its first order - pions. The structure of heavy flavor baryons can be studied within the context of the bound state soliton model. In this approach, hyperons are described as a bound state of an SU(2) topological soliton and a heavy flavored meson. This model is claimed to be able to predict the spectra, electromagnetic properties and coupling constants of the charm hyperons in a remarkable way [15].

The soliton model can be a successful candidate for such an effective theory of QCD in the long-wavelength limit, which is the nonperturbative regime. It is natural to use this model to obtain further insight into the possibility of stable exotic baryons [6]. The authors of reference [6] use two sets of parameters: SET I in which $m_\pi = 0$, and SET II in which $m_\pi = 139$ MeV. The pentaquark is predicted to lie at 2860 MeV (47 MeV binding energy) according to SET II parameters, while SET I predicts that it will lie at 2949 MeV which is 42 MeV above the D_sN threshold.

It is important to note that the soliton model predicts the existence of a non-strange pentaquark: $\bar{Q}qqqq$ where Q stands for c or b quark, and q for u or d quark. This pentaquark is predicted to be bound by 110-190 MeV according to SET I/II respectively. However, this structure is highly unbound according to simple chromomagnetic models which demands the presence of a strange quark in order to have a bound system.

An attempt to evaluate the full Hamiltonian (see equation 2.14) was carried out by Fleck, Gignoux, Richard and Silvestre-Brac [14]. The conclusion is that the pentaquark may not survive a breaking of $SU(3)_F$ symmetry or a finite mass for its charm quark under realistic calculations. In the two-dimensional histogram (fig. 2.4) we see the binding energy of the pentaquark as a function of the mass ratios m_u/m_s and m_u/m_c. The outside surface represents the pure colormagnetic hamiltonian, while the inside surface represents the full hamiltonian (eq. 2.14). The absolute values are too uncertain to decide upon. Thus, it is more reliable to compare between the H and the P, and in that case, the P always retains a larger binding energy than the H.

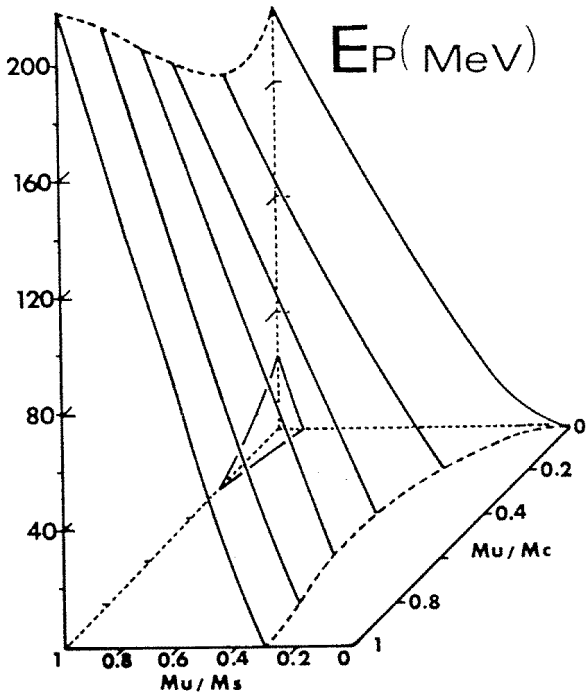

Figure 2.4: Binding energy of the pentaquark as a function of the mass ratios m_u/m_s and m_u/m_c for the pure chromomagnetic Hamiltonian (outside surface) and the full Hamiltonian (inside surface).

2.5 The bag model

The MIT bag model was introduced by the MIT group driven by phenomenological considerations [11]. The original MIT bag describes hadrons as combined from u,d, and s quarks in a cavity. The quark wave functions are given by the free Dirac equation inside a sphere of radius R, acting as gas particles that stand against an external pressure.

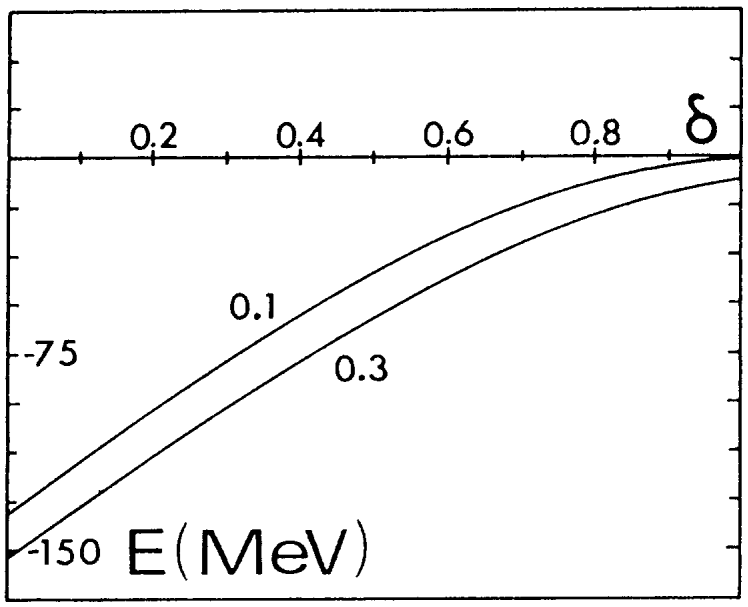

Figure 2.3: The CH binding potential of the P as a function of $\delta = 1 - m_u/m_s$ for two values of $\eta = m_u/m_c$: η =0.1 and η =0.3. We can see that the pentaquark survives the effect of the finite c mass. The pentaquark CH binding potential is approximately 70 MeV for the expected values of δ ($\sim$0.4) and η ($\sim$0.2).

2.4 The full Hamiltonian

The full Hamiltonian is composed of the kinetic energy, the CH binding potential and the Color-Electric central potential. The standard non-relativistic quark Hamiltonian is given by [4]:

$$H = \sum_i (\frac{p_i^2}{2m_i}) - \alpha_E \sum_{i<j} \lambda_i \lambda_j V_{ce}(r_{ij}) - \alpha_S \sum_{i<j} \frac{\lambda_i \lambda_j \vec{\sigma}_i \vec{\sigma}_j}{m_i m_j} V_{ss}(r_{ij}) \tag{2.14}$$

where $V_{ce}(r_{ij})$ represents the Color Electric central potential and $V_{ss}(r_{ij})$ represents the spin-spin interaction. α_E and α_S are the color electric and spin interactions strength, respectively.

Observation of the internal kinetic energy of the system, reveals that when described as a multiquark system the internal kinetic energy of the P is lower then that of the H. Since the P has only 4 light quarks, and one heavy quark - its constituents kinetic energy is lower than the constituents of the H, that contains six light quarks. Consequently, the binding energy of the P may be larger than that of the H.

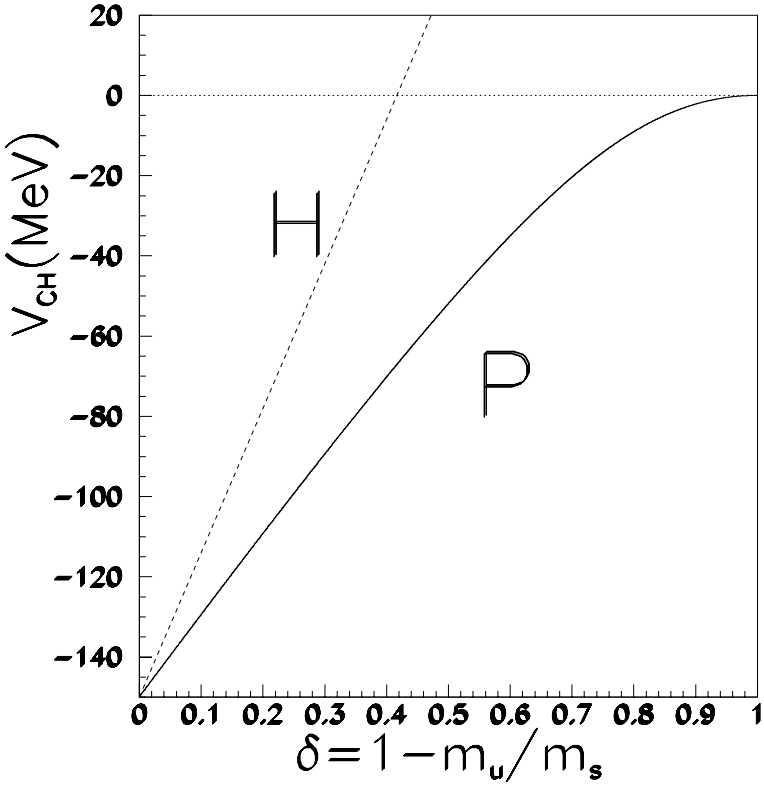

Figure 2.2: The CH binding potential of H(dashed) and P(solid) as a function of $\delta = 1 - m_u/m_s$ values. We can see that for δ =0, which keeps $SU(3)_F$ symmetry the H and the P have the same binding potential of 150 MeV; however, as δ grows, the P survive the $SU(3)_F$ symmetry breaking while the binding potential of the H drops rapidly. The expected value of δ is $\sim$0.4 .

2.3 The effect of finite charm quark mass

In addition to δ, a second parameter $\eta = m_u/m_c$ is introduced in order to take into account the finite mass of the c quark. A study of the effects was carried out by Gignoux [4], using perturbation theory. They show that for $\delta < 0.5$ and the appropriate range for η (0.1-0.3), the binding potential of the P remains almost unchanged-several tens of MeV (see fig. 2.3). It is expected that the value of η is near 0.2 [4].

$$
\begin{aligned}
|P\rangle &= \tfrac{1}{\sqrt{2}}(|n_1;S\rangle + |n_8;S\rangle) \\
|P'\rangle &= \tfrac{1}{\sqrt{2}}(|n_1;S\rangle - |n_8;S\rangle)
\end{aligned}
\tag{2.9}
$$

The eigenvalues of V_{br} in the P and P' frame are calculated to be [10]:

$$
\begin{aligned}
\langle P|V_{br}|P\rangle &= \langle P|V(1-\delta)|P\rangle + \langle P|V_n|P\rangle = \\
&= -16v(1-\delta) + \tfrac{1}{2}\delta(\langle n_1;S|V_n|n_1;S\rangle + \langle n_8;S|V_n|n_8;S\rangle) = \\
&= -16v - 16v\delta + \tfrac{1}{2}\delta(-8v - 2v) = -(16-11\delta)v \\
\langle P'|V_{br}|P'\rangle &= -5\delta v \\
\langle P|V_{br}|P'\rangle &= -3\delta v.
\end{aligned}
\tag{2.10}
$$

Thus, the CH Hamiltonian of the pentaquark under broken $\mathrm{SU}(3)_F$ symmetry $H_{br}(P)$ can be described by the matrix:

$$
H_{br}(P) = -v \begin{pmatrix} 16-11\delta & 3\delta \\ 3\delta & 5\delta \end{pmatrix}
\tag{2.11}
$$

The lowest eigenvalue of this matrix is the CH potential. In order to extract the binding potential, it is necessary to subtract the CH potentials of the threshold $(D_s N)$ which remain unaffected by $\mathrm{SU}(3)_F$ breaking (The nucleon doesn't possess any strange quark, while the D_s has a negligible CH interaction due to the heavy mass of the c quark).

Similar arguments with respect to the hexaquark lead to $H_{br}(H)$ [10]:

$$
H_{br}(H) = -v \begin{pmatrix} 24-16\delta-3\delta^2 & -\delta^2/\sqrt{3} \\ -\delta^2/\sqrt{3} & -8+16\delta-\frac{11}{3}\delta^2 \end{pmatrix}
\tag{2.12}
$$

In order to extract the binding potential of the H, it is necessary to subtract the CH potentials of the threshold $(\Lambda\Lambda)$.

In figure 2.2 the CH binding potentials of the hexaquark and pentaquark appear as functions of δ [4]. We can see that the P state survives a strong breaking of $\mathrm{SU}(3)_F$ much better than the H.

Analysis of the mass splittings between Λ,Σ, and Σ^* leads to the following estimate for δ [4]:

$$
\delta = \frac{3(\Sigma-\Lambda)}{2\Sigma^* + \Sigma - 3\Lambda} \approx 0.37
\tag{2.13}
$$

Moreover, according to reference [4] there is evidence that in the neighborhood of heavy quarks $\mathrm{SU}(3)_F$ symmetry is restored (i.e., $\delta \approx 0$).

and the hexaquark have the same binding color hyperfine potential of 150 MeV. Figure 2.1 illustrates the hyperfine mass splittings.

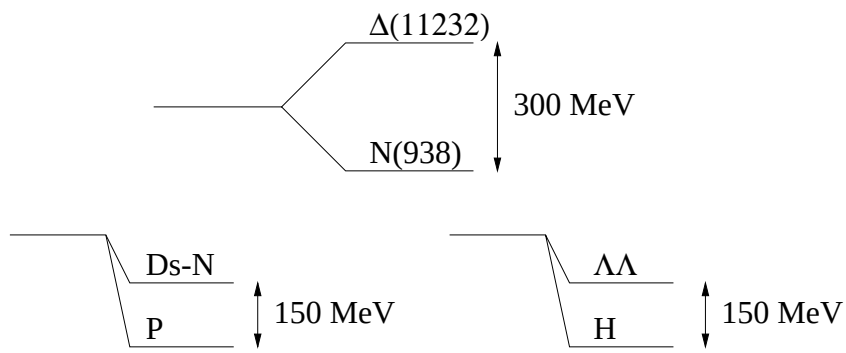

Figure 2.1: The 300 MeV Δ-N mass splitting is equivalent to $16v$ (top). The $P - D_s$ (bottom left) and H$-\Lambda\Lambda$ (bottom right) have both hyperfine splitting of $8v$, equivalent to 150 MeV binding potential.

2.2 The effect of SU(3)$_F$ symmetry breaking

In order to get a more realistic estimate, one must correct for SU(3)$_F$ symmetry breaking [4]. The introduction of SU(3)$_F$ breaking has been shown to reduce the binding potential of the H as well as of the P [3]. This can be seen by noting that the hyperfine binding potential of both H and P is reduced because the color-magnetic interaction of the strange quark is becoming smaller as its mass grows.

The effect of m$_s$ can be parameterized by $\delta = 1 - m_u/m_s$. The broken SU(3)$_F$ symmetry can be written as:

$$V_{br} = V(1-\delta) + \delta V_n \tag{2.7}$$

where: V is the CH interaction under SU(3)$_F$ symmetry, V_n is the CH interaction acting between u,d quarks only, and V_{br} is CH interaction under the broken symmetry.

The eigenfunctions of the CH interaction V$_n$ are states in which the colors of the three non-strange quarks are coupled to either a singlet $|n_1; S\rangle$ or an octet $|n_8; S\rangle$:

$$\begin{aligned} &\langle n_1; S|V_n|n_1; S\rangle = V(N) = -8v \\ &\langle n_8; S|V_n|n_8; S\rangle = -2v \qquad\qquad [C_6(70) = 66, C_3(8) = 12, S = \tfrac{1}{2}, N = 3]. \end{aligned} \tag{2.8}$$

The states $|n_1; S\rangle$, $|n_8; S\rangle$ can be described as linear combinations of SU(6)$_{colorspin}$ states $|P\rangle$ and $|P'\rangle$:

where C_6,C_3 are the eigenvalues of the $SU(6)_{colorspin}$ and $SU(3)_{color}$ Casimir operators, respectively. S is the total spin of the system and N_q is the number of quarks.

In order to evaluate the hyperfine interaction for different hadrons, a quantum state can be defined using the form:

$$|d_6, d_3, S, N\rangle \tag{2.5}$$

where d_6 and d_3 denote the dimension of $SU(6)_{colorspin}$ and $SU(3)_{color}$ respectively. Table 2.1 lists the quantum state of a number of particles (as defined by eq. 2.5), as well as the Casimir operators C_6 and C_3.

Table 2.1: The quantum state $|d_6, d_3, S, N\rangle$ and Casimir operators $C_6(d_6)$ and $C_3(d_3)$ for a number of particles (charmed quarks are ignored).

$\|N\rangle = \|\Lambda\rangle = \|70, 1, 1/2, 3\rangle$	$C_6(70) = 66$	$C_3(1) = 0$	$S = \frac{1}{2}$	$N = 3$
$\|\Delta\rangle = \|20, 1, 3/2, 3\rangle$	$C_6(20) = 42$	$C_3(1) = 0$	$S = \frac{3}{2}$	$N = 3$
$\|H\rangle = \|490, 1, 0, 6\rangle$	$C_6(490) = 144$	$C_3(1) = 0$	$S = 0$	$N = 6$
$\|P\rangle = \|210, 3, 0, 4\rangle$	$C_6(210) = \frac{304}{3}$	$C_3(3) = \frac{16}{3}$	$S = 0$	$N = 4$

Substituting the above in equation 2.4 gives:

$$\begin{aligned}
V_{CH}(N) = V_{CH}(\Lambda) &= -\tfrac{1}{2}v[66 - \tfrac{8}{3}\cdot\tfrac{3}{4} - 48] &= -8v \\
V_{CH}(\Delta) &= -\tfrac{1}{2}v[42 - \tfrac{8}{3}\cdot\tfrac{15}{4} - 48] &= +8v \\
V_{CH}(H) &= -\tfrac{1}{2}v[144 - 96] &= -24v \\
V_{CH}(P) &= -\tfrac{1}{2}v[\tfrac{304}{3} - \tfrac{16}{3} - 64] &= -16v.
\end{aligned}$$

Assuming $SU(3)_F$ symmetry ($m_u = m_d = m_s$), and neglecting the contribution of the charm quark, which is very heavy compared with the u,d, and s quarks, the color hyperfine potential of the pentaquark is $V_{CH}(P) = -16v$. In order to evaluate the binding potential of the system, one must subtract the V_{CH} of the lightest color singlet (see section 2.9) of which the pentaquark (hexaquark) is composed of - $D_s N$ ($\Lambda\Lambda$), from the V_{CH} of the P (H). The color hyperfine interaction of the D_s is negligible due to the heavy charm quark, and therefore:

$$\begin{aligned}
Binding - Potential(P) = V_{CH}(P) - V_{CH}(N) &= -16v + 8v &= -8v. \\
Binding - Potential(H) = V_{CH}(H) - 2V_{CH}(\Lambda) &= -24v + 16v &= -8v.
\end{aligned} \tag{2.6}$$

The value of v can be determined from the 300 MeV Δ - N mass splitting: $V_{CH}(N) = -8v$; $V_{CH}(\Delta) = +8v$. At this point it appears that the pentaquark

Chapter 2

Theory

2.1 The pentaquark binding potential

The Color Hyperfine (CH) interaction between quarks of mass m, spin σ and color λ^α can be written as:

$$V_{CH} = -v \sum_{i>j} \sum_{\alpha} \frac{\lambda_i^\alpha \lambda_j^\alpha \vec{\sigma}_i \vec{\sigma}_j}{m_i m_j} \tag{2.1}$$

where the coefficient v stands for the strength of the interaction. The summation is over all quark pairs (i,j) and three colors (α).

Since in the denominator appears the product of the two quark masses, heavier quarks contribution can be neglected. Therefore, we are left only with interaction among light quarks u,d, and s. Under SU(3)$_F$ symmetry $m_u = m_d = m_s$ leading to:

$$V_{CH} = -\frac{v}{m_u^2} \sum_{i>j} \sum_{\alpha} \lambda_i^\alpha \lambda_j^\alpha \vec{\sigma}_i \vec{\sigma}_j \tag{2.2}$$

The summation is natural under the colorspin representation of SU(6).
The 35 generators of the SU(6) are:

$$\{\alpha\} = \left\{ \begin{array}{c} \frac{\sqrt{2}}{3}\sigma^k \\ \lambda^\alpha \\ \sigma^k \lambda^\alpha \end{array} \right\} \tag{2.3}$$

where σ^k are Pauli matrices ($k = 1, 2, 3$) and λ^α are Gell-Mann matrices ($\alpha = 1...8$). Equation 2.2 can be reduced to [1]:

$$V_{CH} = -\frac{1}{2} v [C_6 - C_3 - \frac{8}{3} S(S+1) - 16 N_q] \tag{2.4}$$

between signal and background events. At the end of the chapter several studies that helped lowering the amount of background (Misidentification study and ghost tracks) are shown.
In chapter 6 the results are reported including their statistical and systematic errors. The upper limit is evaluated as well as its lifetime dependence.
Chapter 7 compares the present results to other pentaquark studies, and chapter 8 summaries the thesis.

extended the soliton model to the heavy flavor sectors by considering a bound SU(2) topological soliton state and a heavy meson. Their study shows that not only the charmed strange (c=-1,s=1) pentaquark states $[u, d, d, s, \bar{c}]$, $[u, u, d, s, \bar{c}]$ are stable, but also the charmed (c=-1,s=0) pentaquark $[u, u, d, d, \bar{c}]$ is stable. More work on pentaquark based on the soliton model is described in [7].

One of the latest theoretical works on the pentaquark was carried out by Takeuchi, Nussinov and Kubodera [8]. The authors applied the instanton-induced interactions to the hexaquark and pentaquark and predicted that the hexaquark inner repulsion is stronger than that of the pentaquark. Considering the uncertainties in the intermediate attraction used by the authors, both exotic particles possess low binding potentials, which are not sufficient to definitely predict the existence of either.
If the pentaquark will be discovered, its existence will shed new light on our understanding of QCD and associated models, and will open a path to a new spectroscopy.

The purpose of this thesis was to search experimentally for the existence of the pentaquark, in the framework of experiment E791 [9], conducted at Fermi National Accelerator Laboratory. Experiment E791 is the fourth in a series of fixed target charmed particle experiments, using the same spectrometer that was upgraded over the years. The experiment used a high-rate data acquisition system in order to record 20 billion interactions of 500 GeV/c π^- in platinum and diamond targets. The data was recorded with a low bias transverse energy trigger (E_T). 2×10^5 charm decays were fully reconstructed for high statistic studies of rare charm decay physics and the search for flavor changing neutral currents.

In the following chapter, I describe the theory of the pentaquark state: The binding potential and mass, production mechanisms, and lifetime and decay modes.
In chapter 3 the experimental setup is described with details about the spectrometer silicon micro strip detectors, magnets, drift chambers, proportional wire chambers, Čerenkov counters, calorimeters and the muon system. The trigger that was used in E791 and the fast data acquisition system are also discussed.
In chapter 4 the stripping process used to filter out most of the unwanted events from E791 large data sample is discussed. The Monte Carlo simulation used in order to build an effective stripping program is also described.
In chapter 5 the analysis is described in details. First a brief description of the analysis method is presented, followed by the physics selection criteria used to distinguish

Chapter 1

Introduction

The possible existence of exotic hadrons has been the subject of curiosity for a number of years. Extensive theoretical studies resulted in a few suggestions for such hadrons.

Ordinary hadrons are mesons or baryons, whose quantum numbers can be described by quark-antiquark ($q\bar{q}$) for mesons or three quarks (qqq) for baryon. Hadrons with larger number of quarks are called exotic hadrons and can be described by ($q\bar{q}q\bar{q}$), ($q\bar{q}qqq$),($qqqqqq$), etc. Exotic multiquark states whose quantum numbers cannot be matched by ($q\bar{q}$) or (qqq) differ from crypto-exotic multiquarks (or hybrid, or glueballs) with the same quantum numbers as ordinary hadrons. Jaffe [1] was the first to predict the existence of a bound $[u, u, d, d, s, s]$ system, called "H" (hexaquark) expected to be stable against strong decay. Jaffe used the bag model [2] which provides a way to deal with multiple quark systems in conventional spectroscopy. Applying the bag model onto the six quark system predicts the existence of the relatively light dihyperon.

Subsequently, Lipkin [3] and Gignoux et al. [4] predicted that also systems made out of 5 quarks: $[u, u, d, s, \bar{c}]$ and $[u, d, d, s, \bar{c}]$, will be stable against strong decay. These two particles were called "$P^0_{\bar{c}s}$" and "$P^-_{\bar{c}s}$" respectively, where the P stands for pentaquark. The possible existence of an exotic pentaquark has inspired more scientists to study the subject. One of them is M. Bjornberg, who calculated the magnetic moments and radii of the pentaquark [5].

Although QCD is seen as the elementary theory of strong interactions, our understanding in the low-energy range still remains a challenging problem. One of QCD effective models that describes the hadronic physics in the low momentum transfer region is the soliton model, known also as the Skyrme model. Riska and Scoccola [6] predicted the existence of the pentaquark using the soliton model as well. They

List of Tables

2.1 The quantum state $|d_6, d_3, S, N\rangle$ and Casimir operators $C_6(d_6)$ and $C_3(d_3)$ for a number of particles (charmed quarks are ignored). 6

2.2 Major decay modes of the "color-singlet" components of the pentaquark. 16

2.3 The lifetime of some charm particles. 17

3.1 Threshold momenta in the Čerenkov counters 24

3.2 Čerenkov counters light response 24

5.1 Table of selection criteria. 52

6.1 Summary of systematic errors. 65

6.2 Upper Limit Results 67

6.5 DIP systematic error - the difference in the mean value of DIP between MC($P^0_{\bar{c}s}$) and data D^0 is 4.4μ (.00044 cm). The difference between the means of MC(D_s) and data(D_s) is 2.4μ (not shown). The DIP variable was shifted by these amounts to yield a ratio for $\frac{\epsilon(D_s)_{DIP=30-2.4\mu}}{\epsilon(P^0_{\bar{c}s})_{DIP=30-4.4\mu}}$. The difference between this ratio and that using the original values of selection criteria was taken as the systematic error (+0.3%). 62

6.6 Č(K1) (first kaon Čerenkov) systematic error - the difference in the mean value of Č(K1) probability between MC(D_s) and data D_s is +0.009. The corresponding difference between the means of MC($P^0_{\bar{c}s}$) and data(D_s) is −0.018 (not shown). The Č(K1) variable was shifted by these amounts to yield a ratio for $\frac{\epsilon(D_s)_{C(K1)=0.14+0.009}}{\epsilon(P^0_{\bar{c}s})_{C(K1)=0.14-0.018}}$. The difference between this ratio and that using the original values of selection criteria was taken as the systematic error (−3.8%). The Čerenkov probability of the second kaon has similar distribution (the first kaon is the K^* daughter). 63

6.7 Lifetime dependence of the upper limit. The two top histograms show the decay time distribution from pentaquark MC(2.83 GeV/c^2) truth table at production (left), and under final selection criteria (right). The bottom left plot shows the acceptance ϵ(MC) as a function of lifetime, were ϵ(MC) refer to the detection efficiency of pentaquark in the 2.79-2.83 GeV/c^2 mass region. The bottom right plot shows the upper limit of the same mass range as a function of lifetime. 68

7.1 The $\phi\pi p$ mass spectrum. The expected region for a pentaquark is cross-hatched. Three phase space events of D_s-p and D^0-p are marked with horizontal lines. 69

7.2 The expected ratio $\frac{BR(P^0_{\bar{c}s}\to\phi\pi p)}{BR(P^0_{\bar{c}s}\to K^*Kp)}$ as a function of the pentaquark mass. 72

5.5 Sin(θ) between pairs of secondary vertex tracks. The enhancement in the first bin (Sin(θ) < 0.0001) is due to "Ghost" tracks. 49
5.6 Misidentified signals of $D^0 \rightarrow K\pi\pi\pi$ (top), and $\phi \rightarrow KK$ (bottom), both under the mild selection criteria set. The vertical lines indicates the exact masses of the D^0,ϕ particles. 50
5.7 $KK\pi p$ mass distribution of events that were rejected due to misidentification, plotted under the mild set of selection criteria. 51
5.8 The signals that were used in the optimization procedure: The data D_s at the top row, the data D^0 in the middle row and the MC(pentaquark) at the bottom row. The micro strip cuts are applied in the left column, the mild set is applied in the center column, and the final set is applied in the right column. The D_s selection criteria do not include proton Čerenkov and momentum criteria (marked by '$*$'). The D^0 selection criteria (marked by '$**$') do not include proton and second kaon Čerenkov and momentum criteria. Moreover, the D^0 Pt2DK selection criterion has a value of 0.3 GeV^2/c^2 (instead of 0.4-0.5 GeV^2/c^2) due to its low Q value (the original values eliminate most of the D^0 signal). 54

6.1 The K^*Kp mass spectrum from data under the final selection criteria. The signal region is cross-hatched. Two phase space events of D_s-p and $D^{\pm}$-p are marked with horizontal lines. 56
6.2 A 90% confidence level upper limit on the number of signal events as a function of the expected number of background events. For more details see [22]. 57
6.3 The K^*K mass spectrum from data under the final selection criteria. Two signals can be seen: D_s meson (right) and $D^{\pm}$ meson (left). The background levels on both sides of the D_s signal are not symmetric (see discussion in sec. 6.2). 58
6.4 Two dimensional plot of $K\pi\pi$ versus $KK\pi$ invariant masses. The $K\pi\pi$ invariant mass reveals a misidentified $D^{\pm} \rightarrow K\pi\pi$ signal. This histogram has exactly the same entries as the previous one. 59

5.1 Illustration of some of the variables. A π^- particle (left side) hits one of the target foils (gray). The pentaquark production vertex (primary) is located within the target foil (dark), while the decay vertex (secondary) is located outside of the target foil (dark ellipsoid on the right). The four pentaquark daughter tracks (K,K,π,p) originating from the secondary vertex, can be seen on the right side. The notations "pri" and "sec" stands for the primary and secondary vertices, respectively. . . 39

5.2 Optimization of the selection criterion for the DIP parameter. DIP taken from pentaquark(MC) appear on the left while DIP taken from D^0(Data) appear on the right. From top to bottom appear the DIP efficiency, sensitivity and the product of efficiency and sensitivity. The dashed vertical line indicates the DIP selection criterion chosen for the mild set of selection criteria, placed at the peak of the product of efficiency and sensitivity (0.004 cm). The solid line indicates the DIP selection criterion chosen for the final set of selection criteria, placed at the peak of sensitivity (0.003 cm). All histograms are plotted under the micro strip set of selection criteria. 44

5.3 Optimization of the selection criterion for the kaon Čerenkov parameter. Kaon Čerenkov taken from pentaquark(MC) appear on the left while kaon Čerenkov taken from D_s(Data) appear on the right. From top to bottom appear the kaon Čerenkov efficiency, sensitivity and the product of efficiency and sensitivity. The solid vertical line indicates the kaon Čerenkov selection criterion chosen for the final set, which remains unchanged from its micro strip level at 0.14. All histograms are plotted under the micro strip set of selection criteria. 45

5.4 Optimization of the selection criterion for the Pt2DK parameter. From top to bottom appear the Pt2DK efficiency, sensitivity and the product of efficiency and sensitivity. Pt2DK taken from the pentaquark(MC) sample of 2.83 GeV/c^2 appear on the left, while Pt2DK taken from the pentaquark(MC) sample of 2.75 GeV/c^2 appear on the right. The dashed vertical line indicates the Pt2DK selection criterion of the mild set, placed at the peak of the product of efficiency and sensitivity. The solid line indicates the Pt2DK selection criterion chosen for the final set, placed at the peak of sensitivity for pentaquark of the mass of 2.75 GeV/c^2. All histograms are plotted under the micro strip set of selection criteria. 47

List of Figures

2.1 The 300 MeV Δ-N mass splitting is equivalent to $16v$ (top). The $P-D_s$ (bottom left) and H$-\Lambda\Lambda$ (bottom right) have both hyperfine splitting of $8v$, equivalent to 150 MeV binding potential. 7

2.2 The CH binding potential of H(dashed) and P(solid) as a function of $\delta = 1 - m_u/m_s$ values. We can see that for δ =0, which keeps SU$(3)_F$ symmetry the H and the P have the same binding potential of 150 MeV; however, as δ grows, the P survive the SU$(3)_F$ symmetry breaking while the binding potential of the H drops rapidly. The expected value of δ is $\sim$0.4 9

2.3 The CH binding potential of the P as a function of $\delta = 1 - m_u/m_s$ for two values of $\eta = m_u/m_c$: η =0.1 and η =0.3. We can see that the pentaquark survives the effect of the finite c mass. The pentaquark CH binding potential is approximately 70 MeV for the expected values of δ ($\sim$0.4) and η ($\sim$0.2). 10

2.4 Binding energy of the pentaquark as a function of the mass ratios m_u/m_s and m_u/m_c for the pure chromomagnetic Hamiltonian (outside surface) and the full Hamiltonian (inside surface). 11

2.5 Feynman diagrams of the decays $P^0_{\bar{c}s} \to \phi\pi p$ and $P^0_{\bar{c}s} \to K^*Kp$. 16

3.1 The E791 Spectrometer. 21

3.2 The Čerenkov probability of MC protons. The distribution shows the a-priori peak at 0.04, the proton-Kaon ambiguity peak at 0.25, and a positive proton identification peak at 1.00. 25

3.3 The Pretrigger 28

4.1 Data reduction diagram 33

7 Other pentaquark searches **69**

7.1 Estimate of the ratio $\frac{BR(P^0_{\bar{c}s} \to \phi \pi p)}{BR(P^0_{\bar{c}s} \to K^* K p)}$ 70

7.2 Expected ratio of observed events 72

8 Summary **74**

4.3 The generic Monte Carlo 34

5 The analysis **36**

5.1 Selection of the decay channel 36
5.2 Method of analysis 37
5.3 The analyzer 38
5.4 Analysis parameters 38
5.4.1 SDZ 39
5.4.2 ISO 39
5.4.3 DIP 40
5.4.4 DIP(K^*) 40
5.4.5 DCA 40
5.4.6 Pt2DK 40
5.4.7 Pt balance 40
5.4.8 RAT, RATi, RATi/AVER 41
5.4.9 Vertex χ^2 41
5.4.10 Seed 41
5.5 Determination of selection criteria 42
5.5.1 Optimization example: The DIP parameter 43
5.5.2 Optimization example: The kaon Čerenkov parameter 45
5.5.3 Optimization example: The Pt2DK parameter 46
5.6 Additional selection criteria 48
5.6.1 Tracks 48
5.6.2 Vertices 48
5.6.3 The Čerenkov mirror gap (baffle) 48
5.6.4 Ghost tracks 49
5.7 Misidentification of particles 49
5.8 Table of selection criteria 52

6 Results **55**

6.1 Upper limit for Poisson processes 57
6.2 The D_s signal 58
6.3 Statistical errors 60
6.4 Systematic errors 60
6.5 Evaluation of the upper limit 65
6.6 Lifetime dependence 67

Contents

1 Introduction **2**

2 Theory **5**

2.1 The pentaquark binding potential 5
2.2 The effect of $SU(3)_F$ symmetry breaking 7
2.3 The effect of finite charm quark mass 9
2.4 The full Hamiltonian 10
2.5 The bag model 11
2.6 The soliton model 12
2.7 The instantons model 13
2.8 Production mechanisms 13
2.9 Expected decay modes of the pentaquark 15
2.10 Expected lifetime of the pentaquark 17

3 The experiment **19**

3.1 The E791 spectrometer 21
3.1.1 Silicon microstrip detectors 21
3.1.2 Magnets 22
3.1.3 Drift chambers 22
3.1.4 Proportional wire chambers 22
3.1.5 Threshold Čerenkov counters 23
3.1.6 Calorimeters 26
3.1.7 Muon detection 26
3.2 The trigger 27
3.3 Data acquisition 28

4 The data sample **30**

4.1 Data processing 30
4.2 The pentaquark Monte Carlo 34

Acknowledgments

I would like to express sincere thanks to my advisor Professor Ashery, who taught me many aspects of becoming an experimental physicist. His guidance, advice and support, while allowing a high level of independence in work, were very important to me.

I would like to thank all members of the E791 collaboration. Without them this work could not have been performed. Their patience and experience helped me a lot. I would like to thank Professor Harry Lipkin from the Weizmann institute, for his theoretical guidance.

Special thanks to the Nuclear Physics group of Tel-Aviv university: the professors, my fellow students, Moshe Zilca the technician and our secratery Riki Cohen. They all made the university life pleasant. Very special thanks to Sharon MayTal Beck, a dear fellow student that started the search for the pentaquark (in a closely related decay channel). Sharon's knowledge and experience helped me a lot and eased my entrance into the E791 experiment.

Finally I want to thank my parents for making me what I am today, and my wife Tali, for her love and support.

This research was supported by the U.S.Israel Binational Science Foundation, the Israel Science Foundation founded by the Israel Academy of Sciences and Humanities and by the U.S. Department of Energy.

Abstract

The strange-anticharmed pentaquark is a doublet of states: $P^0_{\bar{c}s} = |\bar{c}suud\rangle$ and $P^-_{\bar{c}s} = |\bar{c}sudd\rangle$, predicted to be stable against strong and electromagnetic decay.

A search for the pentaquark was carried out by the E791 collaboration. The fixed target experiment E791 was performed at Fermi National Accelerator Laboratory. It collected over $2{\cdot}10^{10}$ π^--nucleus interactions and fully reconstructed more then $2{\cdot}10^5$ charm decays.

In this work the search for the pentaquark in the $P^0_{\bar{c}s} \rightarrow K^*Kp$ decay mode is described. The search objective to reach a sensitivity level of a few percent of that required to detect the D_s meson was achieved. However, no signal above the background was found. Consequently, upper limits on the ratio $\frac{\sigma \times BR(P^0_{\bar{c}s} \rightarrow K^*Kp)}{\sigma \times BR(D_s \rightarrow K^*K)}$ are given with a 90% Confidence Level (C.L.). The upper limits have strong dependence on the (unknown) lifetime of the pentaquark. Assuming a pentaquark lifetime of 0.4 psec, the 90% C.L. upper limits are 0.036, 0.018, 0.016 and 0.019 for pentaquark masses of 2.75-2.79 GeV/c^2, 2.79-2.83 GeV/c^2, 2.83-2.87 GeV/c^2, and 2.87-2.91 GeV/c^2, respectively. These limits include corrections due to statistical and systematic errors.

This work was carried out under the supervision of

Prof. Daniel Ashery

Search for the Pentaquark via the Decay $P^0_{\bar{c}s} \to K^* K p$

THESIS SUBMITTED FOR THE DEGREE
"DOCTOR OF PHILOSOPHY"

by

Gilad Hurvits

SUBMITTED TO THE SENATE OF TEL-AVIV UNIVERSITY

December 1997